Location-aware ingestible microdevices for wireless monitoring of gastrointestinal dynamics

Saransh Sharma[1,9], **Khalil B. Ramadi**[2,3,4,5,9], **Nikhil H. Poole**[1], **Shriya S. Srinivasan**[3,6], **Keiko Ishida**[2], **Johannes Kuosmanen**[2], **Josh Jenkins**[2], **Fatemeh Aghlmand**[1], **Margaret B. Swift**[7], **Mikhail G. Shapiro**[7,8,10], **Giovanni Traverso**[2,3,10], **Azita Emami**[1,8,10]

[1]Department of Electrical Engineering, California Institute of Technology, Pasadena, CA, USA.

[2]Department of Mechanical Engineering, Massachusetts Institute of Technology, Cambridge, MA, USA.

[3]Division of Gastroenterology, Hepatology and Endoscopy, Department of Medicine, Brigham and Women's Hospital, Harvard Medical School, Boston, MA, USA.

[4]Division of Engineering, New York University Abu Dhabi, Abu Dhabi, UAE.

[5]Tandon School of Engineering, New York University, New York, NY, USA.

[6]Koch Institute for Integrative Cancer Research, Massachusetts Institute of Technology, Cambridge, MA, USA.

[7]Department of Chemical Engineering, California Institute of Technology, Pasadena, CA, USA.

[8]Andrew and Peggy Cherng Department of Medical Engineering, California Institute of Technology, Pasadena, CA, USA.

[9]These authors contributed equally: Saransh Sharma, Khalil B. Ramadi.

[10]These authors jointly supervised this work: Mikhail G. Shapiro, Giovanni Traverso, Azita Emami.

Abstract

Localization and tracking of ingestible microdevices in the gastrointestinal (GI) tract is valuable for the diagnosis and treatment of GI disorders. Such systems require a large field-of-view of tracking, high spatiotemporal resolution, wirelessly operated microdevices and a non-obstructive field generator that is safe to use in practical settings. However, the capabilities of current systems remain limited. Here, we report three dimensional (3D) localization and tracking of wireless ingestible microdevices in the GI tract of large animals in real time and with millimetre-scale resolution. This is achieved by generating 3D magnetic field gradients in the GI field-of-view using high-efficiency planar electromagnetic coils that encode each spatial point with a distinct magnetic field magnitude. The field magnitude is measured and transmitted by the miniaturized, low-power and wireless microdevices to decode their location as they travel through the GI tract. This system could be useful for quantitative assessment of the GI transit-time, precision targeting of therapeutic interventions and minimally invasive procedures.

Localization and tracking of wireless microdevices in the gastrointestinal (GI) tract with high spatiotemporal accuracy is of high clinical value[1]. It can enable the continuous monitoring and transit-time evaluation of the GI tract, which is essential for accurate diagnosis, treatment and management of GI motility disorders such as gastroparesis, ileus and constipation[2,3]. GI motility disorders are also increasingly associated with a variety of metabolic and inflammatory disorders such as diabetes mellitus and inflammatory bowel disease. Together, these GI disorders affect more than one-third of the population globally and impose a considerable burden on healthcare systems[3]. High resolution and real-time tracking of wireless microdevices in the GI tract can also benefit anatomically targeted sensing and therapy, localized drug delivery, medication adherence monitoring, selective electrical stimulation, disease localization for surgery, three-dimensional (3D) mapping of the GI anatomy for pre-operative planning and minimally invasive GI procedures[1–4].

The current gold-standard solutions for these procedures include invasive techniques such as endoscopy and manometry, or procedures that require repeated use of potentially harmful X-ray radiation such as computerized tomography (CT) and scintigraphy[1–5]. These techniques also require repeated evaluation in a hospital setting, which can confound observations given the recognized variability in motility and activity. Ideally, GI monitoring would be carried out in real-world ambulatory settings through portable and non-invasive procedures without causing patient discomfort. Alternative approaches—including video capsule endoscopy (VCE) and wireless motility capsules—allow monitoring of the GI tract in real-world settings without interruption to daily activities[6–11]. Wireless motility capsules are orally administered and track the pH, pressure and temperature along the GI tract, whereas VCE can augment the measurements by also acquiring video. However, these methods lack direct measurement of the capsule's location in the GI tract, which needs to be inferred from the acquired data, thus allowing only large-scale organ mapping[6–8]. X-ray radiographs, in comparison, can measure the ingested capsule's real-time location with an accuracy of

around 500 μm[12]. Another drawback of VCE is the limited acquisition time of 12 h, which is much shorter than the total GI transit time (around 24–72 h)[6–8].

Electromagnetic (EM)-field-based tracking approaches have also been reported for the localization of sensors and devices in vivo. Two-dimensional (2D) localization of a magnetic sensor in a field-of-view (FOV) spanning less than 2 cm has been achieved using magnetic field gradients generated by bulky permanent magnets[13]. However, the sub-Tesla-level magnetic field produced by permanent magnets in this approach poses a high safety risk when magnetic materials are used in the vicinity. Alternative approaches that localize a magnet moving through the GI tract using an external array of magnetic sensors have also been explored[14–18] but have insufficient FOV and poor spatial resolution, which sharply degrades with using multiple magnets. Commercial systems using EM-based tracking of sensors have also been developed[19,20]. However, the simultaneous requirements of high FOV, planarity and efficiency of the field generator, safety with magnetic materials and metals, fully wireless operation and miniaturization of the devices, high spatiotemporal resolution, automized and real-time data analysis and system scalability with the number of devices have not been met by existing systems in the context of GI monitoring.

In this Article, we report a platform for localizing and tracking wireless microdevices inside the GI tract in real time and in non-clinical settings, and with millimetre-scale spatial resolution and without using any X-ray radiation. This is achieved by creating 3D magnetic field gradients in the desired FOV using high-efficiency planar coils, which uniquely encode each spatial point. It is challenging to generate 3D field gradients using planar EM coils in the absence of a strong background field. We overcome this by employing gradients in the total magnitude of the magnetic field instead of only the Z component, and by using a combination of gradient fields to produce monotonically varying field magnitudes in a large and scalable FOV. We design miniaturized and wireless devices—termed ingestible microdevices for the anatomical mapping of GI tract (iMAG)—to sense and transmit their local magnetic field to an external receiver. The receiver maps the field data to the corresponding spatial location, allowing real-time position tracking of the iMAG devices as they move through the GI tract. Although the concept of frequency encoding similar to magnetic resonance imaging (MRI) has been previously explored[13], we use direct spatial encoding with magnetic field gradients to create a more accurate and energy-efficient system (Supplementary Fig. 1).

System concept

Our system uses high-efficiency planar EM coils to generate 3D magnetic field gradients in an FOV spanning the entire GI tract (Fig. 1). The field gradients are generated in a time-multiplexed sequence such that at any given time, the principal magnetic-field gradient occurs along a single axis. Using the field measurements along three orthogonal axes, the 3D position of the device can be unambiguously decoded. The complete iMAG system can be readily deployed in various non-clinical settings such as smart toilets, wearable jackets or portable backpacks, thus allowing real-time GI tract monitoring without disrupting the daily activities of the patient. A prototype animal chute with gradient coils is designed in this work for evaluation in large animal models, as discussed later. Another prototype with

the gradient coils attached to a toilet seat is designed for an at-home system (Extended Data Fig. 6), demonstrating the use of our technology for chronic and non-invasive human applications.

The spatial localization resolution obtained by our system in each dimension (Δx) is given by

$$\Delta x = \Delta B / G, \tag{1}$$

where ΔB is the iMAG's field-measurement resolution and G is the applied magnetic field gradient along the corresponding axis. The goal for the iMAG is to have $\Delta B = 3\ \mu$T and $G > 3$ mT m^{-1} across the entire FOV to achieve a localization resolution of 1 mm. To localize the devices along each axis (Fig. 2a), a monotonically varying magnetic field is generated that has a gradient in its total magnitude along the same axis. A simplified view for the X axis is shown in Fig. 2b that results in equation (2). The three orthogonal components of the field ($\hat{x}B_x$, $\hat{y}B_x$, $\hat{z}B_x$) measured by each device (Fig. 2b) are used for computing the field magnitude at the device's location, as described in equation (3). The field magnitude can then be mapped to the corresponding spatial coordinate.

$$\|B_{X_1}\| < \|B_{X_2}\| < \|B_{X_3}\|, \tag{2}$$

$$\|B_{X_{i,i=1,2,3}}\| = \sqrt{(\hat{x}B_{X_i})^2 + (\hat{y}B_{X_i})^2 + (\hat{z}B_{X_i})^2} \tag{3}$$

Since the magnetic field B_x has a net gradient in its magnitude along the X axis, G_x is defined as

$$X - \text{Gradient} = G_x = \partial\|B_x\|/\partial x. \tag{4}$$

The process is then repeated for the Y and Z axes to localize the devices along them. By employing gradients in the magnitude of the field along each axis, our localization technique is immune to potential inaccuracies caused by device misalignment relative to any coordinate system.

iMAG design and characterization

We designed the 3D magnetic-field-sensing iMAG devices with the following specifications: high-resolution field measurement (3 μT per least significant bit or LSB); wireless operation at 2.4 GHz Bluetooth frequency; ultralow power for prolonged battery life (2–4 weeks); small form factor (20 mm length and 8 mm diameter) and biocompatibility. The iMAG device (Fig. 2c–e) consists of a 3D magnetic sensor that can measure and digitize magnetic field values to a 16-bit digital vector with 3 μT accuracy (Methods). A Bluetooth low-energy (BLE) microprocessor interfaces with the sensor over the inter-integrated circuit (I2C) protocol. The digitized field vectors received by the microprocessor are sent to a 2.4 GHz Bluetooth antenna for wireless transmission to the external receiver. Coin-cell batteries are used for power. The iMAG is fabricated by assembling these low-cost and commercially available components on a custom-designed printed circuit board (PCB) and packaged into

a biocompatible polydimethylsiloxane mould with the size of an ingestible 000 capsule (Fig. 2f). Supplementary Fig. 15 summarizes the power consumption of the iMAG under different operating modes. The transmit power was set to 4 dBm to ensure maximum connectivity with the receiver. An advertising rate of 2.5 s and a connection interval of 50 ms were chosen as a compromise among the connection speed, stability and battery life. All non-necessary peripherals were deactivated to ensure that the maximum continuous current was within the discharge limits of the battery.

To measure the 3D location of the iMAG, an external smartphone sends a wireless ping signal to an nRF52 development board, used as the receiver in this work (Fig. 2g). The ping signal is relayed by the receiver to the iMAG devices to trigger magnetic field measurements at their appropriate times (Fig. 2h). With its input/output pins connected to the gradient coils' ENA (enable) switches, the receiver also activates the required sequence of coil combinations to generate the magnetic field gradients. On reception of the measured magnetic-field data values from the connected iMAGs (Fig. 2i), the receiver displays them on a computer screen using the universal asynchronous receiver/transmitter (UART) protocol. The receiver concurrently runs a search algorithm to retrieve the 3D spatial coordinates corresponding to the magnetic field data (Methods). The magnetic field value at each point in the FOV is measured and stored in a look-up table (LUT) during a prior characterization phase (Methods). The search algorithm uses the LUT from the characterization phase for position retrieval.

The communication range is defined as the longest distance between the iMAG and receiver before losing connection (when received signal strength at the receiver is less than −96 dBm), and is evaluated under various in vitro settings. First, the iMAG was submerged in an HCl solution to mimic the acidic and fluid-filled gastric cavity. For a pH of 2–6, the range was >1 m (Fig. 2j). For a typical gastric pH from 1.2 to 3.5, the range varied from 30 cm to >1 m, respectively. At lower pH values, the concentration of the freely dissociated H^+ and $Cl^−$ ions increases exponentially in the solution. These ions absorb the 2.4 GHz radio-frequency (RF) signal, with the absorption being proportional to the ionic concentration, and lead to a lower signal strength at the receiver[21]. Intestinal pH is 4.5–6.5, for which the range was >1 m. Second, the range was tested in different concentrations of NaCl solution (saline). For an NaCl concentration of 0.2% w/v (similar to gastric fluid), the range was >1 m (Fig. 2k). For NaCl concentrations from 0.6 to 1.0% w/v (similar to intestinal fluid), the range varied from 60 cm to >1 m, respectively. Third, the range obtained in simulated gastric fluid (SGF) was >50 cm up to 250 ml SGF (Fig. 2l). Finally, the range in simulated intestinal fluid (SIF) was >1 m for up to 250 ml SIF (Fig. 2m) (Methods). Here 250 ml SGF and SIF are chosen as they represent the mean GI fluid volume under fasting and fed conditions[22,23]. We could similarly communicate with the iMAG over 1 m away when placed in 250 ml porcine gastric juice. The next step is to evaluate the communication range under in vivo settings in the presence of several layers of body tissue—skin, fat, muscle and organs—which not only cause the absorption of RF signal by the ionic and dipole concentrations in these layers but also result in multipath reflections due to the heterogeneous nature of tissue[24]. When the iMAG was endoscopically placed in the gastric cavity of an anaesthetized pig, the in vivo range was >1 m. Thus, the iMAG achieves a sufficient communication range for evaluation in a large animal model. For evaluating the

communication time, the iMAG was submerged in an HCl solution (pH 1.5) for two weeks, which is towards the higher end of GI transit time in pigs, and was communicated with every few hours (Methods).

EM coils for 3D magnetic field gradients

We designed EM coils to generate the gradients G_X, G_Y and G_Z to be 3 mT m^{-1} across the entire FOV ($40 \times 40 \times 20$ cm^3; Fig. 3a) to ensure a resolution of 1 mm across all the three spatial dimensions. To create a Z-axis gradient in the magnetic field magnitude, a planar circular coil is designed to carry current in the counterclockwise direction (Fig. 3a, Z coil), producing a monotonically decaying magnetic field magnitude as the Z distance from the coil is increased (Fig. 3b). The d.c. current is chosen as 15 A to get $G_Z > 3$ mT m^{-1} at all the boundary planes of the FOV.

The X coil (Fig. 3a) consists of two halves carrying currents in opposite directions to produce a magnetic field B_X that points into (right, negative) and out of (left, positive) the plane. As the magnitude of B_X is computed, the sign information is lost and results in identical values from both the halves, shown below the X coil in Fig. 3a, making 75% of the coil area unusable. Since the Z coil produces an always-positive field (Fig. 3b), it can be used to correct for the non-monotonicity in the X-coil's field[25] (Methods). With both coils simultaneously powered during the X-measurement phase, the resultant magnetic field along the X axis is strictly monotonic over the entire X FOV (Fig. 3c,d). Variations in the X gradient in the FOV (Fig. 3c,d) are explained in Methods. The Y coil is identical to the X coil (Fig. 3a), except for a 90° rotation. During the Y-measurement phase, both Y and Z coils are simultaneously powered (Fig. 3e). Figure 3f shows the fully assembled gradient coils. The Z coil consists of two layers, each with 80 turns, and each elongated half of the X and Y coils consists of two layers, with 68 turns per layer (Extended Data Fig. 1, Embodiment-1).

A major safety consideration of our system is the potential for peripheral nerve stimulation (PNS) resulting from gradient switching by the coils. The 10 ms rise time for the gradients (Fig. 3e) used in this work is much slower than the 0.1–1.0 ms rise time used in fast MRI scanners. The PNS threshold is commonly defined as the peak $d|B|/dt$ value, reported to be 43.0–57.0 T s^{-1} (ref. [26]), which is more than an order of magnitude higher than our peak value of 1.5 T s^{-1} (Fig. 3g). In addition, the PNS effects are considered negligible when the switching time is >5 ms and $|B| < 100$ mT (ref. [27]). Both these metrics are satisfied by our system. Considering the rise time along with the peak $d|B|/dt$ value, the International Electrotechnical Commission thresholds for PNS and cardiac stimulations have a common asymptotic value of 20.0 T s^{-1} at long rise times (>5 ms) (ref. [28]), which is much higher than the 1.5 T s^{-1} gradient switching employed here. Additionally, no mechanical movement was observed in any of the magnetic equipment placed in the vicinity of the coils, ensuring minimal risk due to the induced magnetic force and torque.

Another safety consideration for the gradient coils is the heat generated during measurements. From Fig. 3e, it is evident that a single measurement cycle lasts less than

300 ms. Given the several-hour-long transit through the stomach, small intestine (SI) and colon[2,3,7,8], and 1–2 contractions per minute in each of these organs on average[8], one measurement per minute is sufficient for the accurate monitoring of transit time and motility. For such sparse measurements, the average heat produced in the coils is only 3.3 W, which is easily dissipated by the large coil area. The power, heat, weight and other specifications of the coils are listed under Embodiment-1 (Extended Data Fig. 1d). Although the heat generated is negligible, the transient power during each measurement is 800 W, which is not suitable for portable prototypes. Another challenge for portability is the high weight of the coils. To circumvent these, a more portable-friendly prototype (Extended Data Fig. 1, Embodiment-2) can be fabricated. Using a copper wire with 0.25 mm diameter, almost nine times more turns can be fitted into the same footprint as the current prototype. The large number of turns considerably relax the current requirement, with only 350 mA d.c. current and 0.25 W heat for Embodiment-2, which leads to <0.1 °C rise in the surface temperature during the measurements. However, the mean position resolution is lowered to 7.5 mm, which is still acceptable for localization in the GI tract. For stationary prototypes used in walls or toilet seats, 15 A current-carrying Embodiment-1 can be used for higher accuracy of localization. The coils can also be operated at the theoretically maximum sampling frequency of 3.3 Hz (1/300 ms) for applications requiring a higher refresh rate, and the heat generated can be alleviated by using thermal insulators around the coils.

Spatiotemporal resolution and system characterization

The value of ΔB found experimentally using the 3D magnetic sensor is 15 µT, which corresponds to Δx ranging from <1 mm (when $G > 15$ mT m^{-1}) to 5 mm (when $G = 3$ mT m^{-1}). The iMAG's lowest resolution of 5.0 mm occurs only at the boundary planes of the FOV and is 1.0–2.0 mm elsewhere, resulting in a volume-averaged mean value of 1.5 mm (Extended Data Fig. 2). The precision and repeatability of the gradients play an important role in the error performance. We achieved <5% error in the gradients during each measurement by custom designing a coil controller (Supplementary Fig. 13) and extensive characterization (Methods). For applications requiring a higher spatial resolution, several measurements at a single location can be averaged to reduce the effect of sensor noise[25,29]. The same can be achieved by increasing the gradient G at the cost of higher current and/or more layers of coils. For GI monitoring applications, sub-centimetre resolution is acceptable since the GI system exhibits centimetre-scale relative motion even under still external conditions[30]. The temporal resolution of iMAG is dictated by the total delay between sending a wireless ping and completion of 3D position decoding, which is <300 ms (Fig. 3e), providing sufficiently real-time position update for applications in this work.

We first tested the system in vitro to demonstrate functionality and verify the theoretical localization resolution. The 3D position of a single iMAG submerged in a saline tank was found with respect to the global origin of the coils (0,0,0; Fig. 3a). The error is defined as the difference between the actual and decoded position. The absolute peak and mean error magnitudes in X, Y and Z (Fig. 3h) were   5.0 mm and   1.2 mm, respectively, as the location of the iMAG was uniformly varied in the FOV. To eliminate the fixed reference (global origin), we added another iMAG at a known location in the tank (Supplementary

Fig. 2) to serve as a relative reference for the main iMAG. The peak and mean errors in the decoded distance between the main and reference iMAG were 5.0 mm and 1.4 mm, respectively, at all the locations (Fig. 3i).

We performed in vivo testing and characterization in porcine models as they represent a reliable analogue for human application, given their anatomy and size[31]. A custom wooden chute was designed with two sets of gradient coils, each comprising the *X*, *Y* and *Z* coils (Fig. 4a and Supplementary Figs. 11 and 12). The two coil sets are needed to generate 40 × 40 × 40 cm^3 of FOV spanning the porcine GI tract. Unwanted interference between the fields produced by the two coil sets was eliminated by sequential powering. We tested the system's accuracy in vivo using a test fixture (Fig. 4b) with two iMAG devices positioned a fixed distance apart (81.12 mm). The fixture was endoscopically deployed into the gastric cavity (Fig. 4c). The decoded distance between the two devices was 83.6 ± 0.7 mm, falling within our desired error margin of 5.0 mm (Fig. 4d,e and Supplementary Fig. 3).

In vivo evaluation

We first sought to emulate a real-world setting where an iMAG would be ingested and its position would be tracked relative to a reference iMAG located externally on the skin of the ambulatory animal. The iMAG was endoscopically administered (Fig. 4f) and evaluated on passage to assess the electrical and mechanical integrity. The signal strength detected by the receiver as the ingested iMAG is localized is plotted in Fig. 4g. The signal strength when the iMAG is located in the stomach and SI is –80 to –100 dBm, approaching the noise floor of the receiver when less than –95 dBm. The signal strength increased to over –70 dBm when located in the colon or rectum. The ingested iMAG was localized in different regions of the GI tract: (1) stomach (Fig. 4h), (2) colon (Fig. 4i) and (3) rectum (Fig. 4j). The error in the decoded distance between the ingested and reference iMAG devices, compared with the distance obtained from the X-ray scans, was found to be <5 mm for the stomach (Fig. 4k,l) and rectum (Fig. 4o,p) and <10 mm for the colon (Fig. 4m,n). The in vivo error values reported here are overestimations (Methods). The ingested iMAG devices remained functional on excretion (signal strength of more than −60 dBm), thus confirming their applicability for chronic use (Supplementary Figs. 4–6).

We next investigated the utility of our system in a faecal incontinence (FI) model[32]. To monitor the movement of faeces in the distal colon, our FI model comprised a freely moving iMAG in the lumen of the distal colon and a reference iMAG located on the skin surface near the anal sphincter. The objective was to detect the presence of the moving iMAG when within a specific distance (chosen here as 10 cm) of the anal sphincter. We placed an iMAG 16 cm proximal to the anal sphincter in the colon and fixed two reference iMAG devices externally (Fig. 5a). The iMAG was pulled out in increments of 5 mm, with a measurement being made at every step and the reconstructed trajectory shown in Fig. 5b,c. The consecutive X-ray scans performed during the measurements are shown in Extended Data Fig. 3. When the iMAG was 10 cm inside, the error in the distance between the reference and moving iMAG was <3 mm, which validates the functionality of the system as an accurate (>97%) indicator of defecation. We were also able to map the iMAG trajectory

to successfully reconstruct colonic anatomy (Fig. 5b–g and Extended Data Fig. 5) across multiple animals.

Finally, we evaluated the use of iMAG as an in vivo sensor of pre-labelled locations within the GI tract. We placed magnetic barium beads at a specific location in the colon (Fig. 5d) and used our system to sense when the ingested iMAG passed this location (Fig. 5e). We then mapped the iMAG's trajectory with (Fig. 5f,g) and without (Fig. 5h,i) the barium beads. The highly magnetic beads interfere with the local magnetic field, thus impacting the magnetic field readings by the iMAG. The error in the decoded position was appreciable (>1 cm, Fig. 5h,i) when the iMAG was within 5 cm of the beads, thus demonstrating our system's specificity to magnetic labels. The consecutive X-ray scans performed during the measurements are shown in Extended Data Fig. 4. In a clinical scenario where the location of such labels is unknown, the iMAG can make an additional measurement each time before the gradient coils are switched on. The magnetic field produced by the labels can be sensed by the iMAG and distinguished from the relatively low background Earth's field (<60 μT). A prior anatomy map obtained from an existing imaging modality (X-ray/MRI/CT) that shows the relative location of the labels can be used as an additional reference. We have also evaluated the effect of interference using non-magnetic polyethylene beads for negative control and compared with the interference caused by the magnetic barium beads (Supplementary Fig. 10).

Clinical applications

The real-time and millimetre-scale localization resolution of iMAG holds the potential for important clinical benefit. A quantitative assessment of the GI transit time is vital in the diagnosis and treatment of pathologies related to delayed or accelerated motility such as gastroparesis, Crohn's disease, functional dyspepsia, regurgitation, constipation and incontinence[1–4]. Other applications that could benefit from the high spatiotemporal accuracy of our system are therapeutic interventions like the anatomical targeting for drug delivery, monitoring of medication adherence, delivery of macromolecules and electrical stimulation to specific regions of the GI tract in a wireless fashion[11,33–35].

We have shown our system to be a highly accurate indicator of defecation, which is of clinical significance for patients suffering from FI. An iMAG pill could be ingested with each meal to track its progress through the GI tract in patients with FI. The reference iMAG could be incorporated into 'smart' clothing for monitoring the bowel movements. The successful reconstruction of colonic anatomy (Extended Data Fig. 5) also shows that the iMAG can delineate complex and curved trajectories of the retroperitoneally fixed parts of the GI tract, which are hard to acquire through other imaging modalities (X-ray/CT). To localize the moving iMAG with respect to the patient's anatomical features (like bones, muscles or other relatively fixed internal body parts), a prior scan of the patient with the reference iMAG attached at a known external location can be conducted using the existing imaging modalities such as MRI, CT or X-ray scans. Using this one-time scan, the location of internal organs with respect to the reference iMAG can be known. The reference iMAG can be attached to the patient's skin using a Tegaderm patch (or other adhesives) anywhere

in the abdominal region. The water-resistant patch will ensure that the reference iMAG stays at its location for the duration of the internal iMAG's passage.

We have also demonstrated the iMAG's usage as an in vivo sensor to detect the location of magnetic particles and beads. This approach can be used to label injection sites, polyps, fistulas, stomas or strictures requiring localized therapy, using anatomical markers such as magnetic beads or staples. Additional capabilities could be added to the iMAG devices, enabling them to measure and report pH, temperature, pressure, deliver drug payloads and perform electrical/mechanical stimulation[1,4,36,37]. The stimulation/actuation can be performed after localization of the ingested iMAG in the vicinity of the marker. The in vivo experiment using magnetic beads also demonstrates our system's robustness to field distortion caused by magnetic objects when located sufficiently away (>5 cm in this case) from the devices being localized (Supplementary Fig. 10). Sensing capabilities could enable iMAG to generate a spatiotemporal map for comprehensive patient diagnosis and assisting further in anatomical targeting using the pH and pressure profile. From a consumer electronics standpoint, the iMAG offers the potential for non-invasive and location-specific measurement of physiological markers and vital parameters along the gut, which could be of interest in the field of fitness and smart medicine[36].

Conclusions

Our system offers a high FOV, high spatial resolution in three dimensions and fully wireless operation of the ingestible microdevices (Table 1). It also supports concurrent multidevice usage. We use safe magnetic fields generated by non-obstructive planar electromagnets and have demonstrated system functionality in large animals, illustrating its potential for use in non-clinical settings without the need for harmful radiation.

Prior magnetic tracking systems that localize a moving magnet inside the GI tract use an external array of magnetic sensors to reconstruct the magnet's position[14–18,38]. Since the reconstruction is based on the received magnetic field strength and direction at each sensor's location, it is susceptible to field distortions produced by nearby magnetic materials. As a result, these approaches lack scalability across the number of magnets due to the increasingly distorted field produced by each moving magnet when multiple of them are simultaneously used. For single-magnet localization, the mean spatial resolution is around 5 mm that rapidly degrades to more than 1 cm as the distance from the sensor array is increased to more than 15 cm, thus limiting the effective FOV[39,40]. Furthermore, the size of the magnet required to achieve centimetre-scale precision in GI FOV approaches that of a 000 capsule and is larger than the FDA-approved daily dosed osmotic-controlled release oral delivery system, leaving little room for additional components (for actuation or stimulation) that can be fitted in an ingestible pill with minimal risk of obstruction[41,42].

An EM-induction-based system has been previously reported to excite wireless *LC* coils (used as markers), using an externally located pickup coil array to track the markers[43]. A single marker is composed of three *LC* coils (each measuring $15 \times \phi 4$ mm^3) arranged in a ring fashion to achieve six-dimensional (6D) tracking, rendering a size that is unsuitable for an ingestible device. When a single *LC* coil is used as a marker to fit into an ingestible

footprint, it only achieves five-dimensional (5D) tracking and suffers from an inherent dead-angle problem[43], which makes tracking reliability uncertain. In contrast, iMAG is capable of achieving 6D tracking with the current footprint[25]. The system discussed in the other work[43] is also lacking in vivo evaluation and achieves a lower penetration depth than our work. Furthermore, RF-based localization methods have an order of magnitude lower resolution than our approach due to heavy dependence on body tissue and multipath effects[44]. Their penetration depth is also limited due to heavy attenuation of RF signals by body tissue.

A current limitation of our system is the achievable distance of the receiver board (50 cm) when the iMAG is located deep inside the GI tract. This is due to the thick gastric and intestinal walls that cause excessive loss in the 2.4 GHz RF signal strength. Future devices could use a lower frequency of 401–406 MHz (Medical Implant Communication System band) or 915 MHz (Industrial, Scientific and Medical radio band) for communication to achieve a longer distance from the receiver board to the devices. Tissue absorption is attenuated at lower frequencies, leading to a higher signal strength at the receiver. The overall size of the iMAG could also be reduced by using a custom-designed application-specific integrated circuit (ASIC) that has 3D magnetic sensing and wireless communication capabilities. Such ASICs could be used to create highly miniaturized and low-power devices, which can exploit energy harvesting from GI fluids and eliminate the need for batteries for power[45–47].

Future successful translation of our system will require extensive safety studies in large animal models to enable human trials. From a manufacturing perspective, the iMAG can be mass produced at a low cost per device since all the components are off the shelf and inexpensive. With an ASIC implementation of iMAG, the cost can be further reduced. The iMAG's four-week battery life provides sufficient time for evaluation in chronic settings and can be further enhanced by using higher-energy-density batteries. The EM coils for gradient generation incur a single-time manufacturing cost and can be repeatedly used for iMAG monitoring. The FOV produced by the coils is scalable with the coil size, number of layers and d.c. current used. The coils can also be customized for various patient-specific requirements (Fig. 1). For instance, a conformal coil structure can be made into a jacket or incorporated into a backpack and powered with batteries (Extended Data Fig. 1). The coils can also be attached to a toilet seat (Extended Data Fig. 6) or mounted on a rigid wall for regular motility monitoring of patients not comfortable wearing or carrying the coils. This is especially useful for patients with pre-existing disabilities impeding movement and locomotion. Owing to their complete planarity, the coils can easily slide beneath the bed for GI monitoring during sleep[10]. The iMAG technology could, thus, be used to advance current capabilities in GI tract monitoring, diagnosis and treatment.

Methods

iMAG assembly

The PCB for iMAG was fabricated on a standard four-layer 0.062″ FR4 substrate, measuring 14.0 mm × 7.2 mm. The nRF BLE module (nRF52832-CIAA-R), matching-network circuit, 2.4 GHz antenna (2450AT18B100) and 32 MHz crystal (CX2016DB32000D0WZRC1) were soldered on top, whereas the 3D magnetic sensor

(AK09970N) and the 11 mF storage capacitor (CPH3225A) were soldered on the bottom of the PCB. Two coin-cell batteries (SR626W) are stacked together is series and attached to one end of the PCB (closer to the antenna and away from the sensor). Matching network for interfacing between the nRF module and antenna was designed using simulations in Microwave Office software (V13–03-8415–1-64bit) and later tuned in real time on the fabricated board (due to manufacturing variations) using a microwave vector network analyser (N9918A, Keysight). The final matching-network circuit for the nRF comprises a 1 pF shunt capacitor and a 3.3 nH series inductor, and the matching-network circuit for the antenna comprises a 1 pF shunt capacitor and a 4.7 nH series inductor (Fig. 2c,d). Since transmission through the antenna is the most power-hungry phase of the entire operation, it necessitates that the entire matching-network circuit be very accurately tuned to avoid power losses from the nRF to the antenna (Supplementary Figs. 7–9).

The AKN 3D magnetic sensor is based on the Hall effect, has a 16-bit data out for each of the three-axis magnetic components, high sensitivity (1.1–3.1 μT per LSB) and measurement range (±36 mT), and a footprint of $3.00 \times 3.00 \times 0.75$ mm3. It communicates with the nRF module over the I2C protocol. The sensor consumes 2.2 mA of current for 850 μs in the low-noise mode (1.1 μT per LSB) and 1.5 mA for 250 μs in the low-power mode (3.1 μT per LSB). For the iMAG device, the sensor is operated in the low-power mode. Given the high current consumption by the sensor during field measurements, it is imperative to use a high current drive battery and a large storage capacitor, as done for the iMAG. With future implementations of a low-power complementary-metal–oxide–semiconductor-integrated 3D magnetic sensor, both power and area of the iMAG pill can be drastically reduced.

The SR626W silver oxide batteries were chosen because of their compact size (6.8 mm × 2.6 mm) and high current drive capacity (28 mAh), which is sufficient to power the devices for two continuous weeks. For chronic tests, since we wanted to extend the battery life to four weeks, we used SR927W instead, which measures 9.5 mm × 2.7 mm and has a current drive capacity of 60 mAh (more than twice that of SR626W). Additionally, the BLE antenna 2450AT18B100 (Johanson Technology) was replaced by 0479480001 (Molex) due to the latter's higher gain to help achieve a higher signal strength during the chronic experiments. The resultant increase in the device size to 20 mm × 12 mm was still acceptable for an ingestible electronic.

iMAG configuration

The BLE software for the device was implemented as an event-driven application, with both nRF and magnetic sensor operated in the ultralow-power modes at all times, except for the advertising and magnetic-field measurement phases. A BLE custom service application for the sensor was developed to configure iMAG as a peripheral BLE server. The custom application initializes and instantiates all the necessary BLE service modules and advertising schemes, and reports four data values in a single notification-enabled Generic Attribute Profile (GATT) characteristic: (1) field data measured during the X gradient, (2) field data measured during the Y gradient, (3) field data measured during the Z gradient and (4) temperature value measured by the internal temperature sensor of the nRF integrated circuit.

An nRF52 development kit was used to program the iMAG before encapsulation. The sensor was configured via the I2C interface to operate in the single-measurement mode, with measurement events processed and verified through the interrupt pin (ODINT). Furthermore, the random-access memory of the iMAG's nRF chip was redefined to take into account the added GATT characteristics and services. The low-frequency oscillator configuration was also redefined to redirect all the low-frequency operations to the internal 32.768 kHz *RC* oscillator instead of the external 32.768 kHz oscillator, which was omitted from the iMAG PCB to conserve space. For debugging, the sensor's measurements were logged through a UART terminal program via the UART connection on the nRF52 development kit, which was externally controlled from a smartphone. The debugging interface was disabled in the iMAG before encapsulation with polydimethylsiloxane.

For a completely encapsulated iMAG, the peripheral BLE application first initializes the GATT interface, generic access profile parameters, BLE stack and custom service. It then initializes the 400 kHz I2C interface with the sensor, applies a reset and begins advertising. The transmit power was set to 4 dBm to ensure maximum connectivity with the external client (receiver board). To get a robust system, the speed and stability of the connection between the client and iMAG are of paramount importance. However, the high attenuation of 2.4 GHz BLE signals by body tissue demands a high advertising rate and faster connection interval to maximize the connection probability, resulting in higher power consumption. For the batteries used with the current iMAG (SR626W), an advertising rate of 2.5 s and connection interval of 50 ms were used to achieve two weeks of battery life. Once a BLE connection is established, the iMAG remains in the low-power mode until an external event/notification triggering a measurement is received.

Power optimization for iMAG

Power measurements indicate that the iMAG consumed (1) 10 μA in the idle mode and (2) a maximum spike of 15 mA during the advertising mode with an average of 440 μA across all the three BLE channel transmissions. When connected with the receiver board, the iMAG consumed 120 μA in the standby mode, and an average of 250 μA when requesting a measurement from the magnetic sensor. We minimized the power consumed by the iMAG to ensure that the maximum continuous current was within the discharge limits of the battery. All non-necessary peripherals were deactivated, including the BLE general-purpose input/ output pins, all interrupt pins and general board support package module. Furthermore, d.c./d.c.-mode power management was enabled on iMAG's nRF to make it switch automatically between the on-chip d.c./d.c. regulator and the low-dropout regulator, depending on the instantaneous load. Such a regulation protocol is more power efficient, particularly in the presence of high-power transmit radio spikes. The 10 μH and 15 nH inductors needed for the d.c./d.c.-mode power regulation mechanism were soldered onto the PCB in accordance with the regulator's impedance requirements. This resulted in notable power saving (Supplementary Table 1).

With the above configuration, the iMAG consumed (1) 8 μA in the idle mode and (2) a maximum spike of 8 mA during the advertising mode with an average of 230 μA across all the three BLE channel transmissions. When connected with the receiver board, the

iMAG consumed 80 μA in the standby mode and an average of 180 μA when requesting a measurement from the sensor. Supplementary Table 1 summarizes all the power-related results.

Receiver board configuration

An nRF52 development board (receiver board) is configured as a BLE client that scans, detects and requests data from the target server (iMAG). On detecting the vendor-specific universally unique-identifier service address associated with an iMAG, the central client automatically assigns all the handles representing the *X*, *Y* and *Z* fields, as well as the temperature GATT characteristics, and initializes all the notification-based procedures. Furthermore, the central client application initializes simultaneous advertising events such that an external smartphone can connect to it and remotely activate event notifications (called as 'ping'). The ping signal is relayed by the central client board to the iMAG devices to trigger the magnetic field measurements at their appropriate times (Fig. 2g–i and Supplementary Fig. 15). With its general-purpose input/output pins connected to the gradient coils' ENA (enable) switches, the central client activates the required sequence of coil combinations (Fig. 3e) to generate the magnetic field gradients.

The receiver board is connected to a laptop via USB; using a simple UART protocol, the board displays the received field-data values in real time as they are streamed from the connected iMAGs. All the GATT characteristic tables and byte-array sizes were matched between the server and client to ensure the accurate transmission of all data values. The central client is capable of requesting and receiving data from multiple iMAGs, each at a distinct location in the FOV.

Spatial resolution

The complete definition of the spatial localization resolution (Δx) obtained by our system, in each of the three dimensions, is given by equation (5)[25]:

$$\Delta x = \frac{\Delta B_{\text{eff}}}{G}\left\{1 + \sqrt{\left(\frac{\delta G_{\text{i}}}{G}\right)^2 + \left(\frac{\delta G_{\text{s}}}{G}\right)^2}\right\}, \tag{5}$$

$$\Delta B_{\text{eff}} = \sqrt{\left(\Delta B_i\right)^2 + \left(\Delta B_j\right)^2 + \left(\Delta B_k\right)^2}. \tag{6}$$

Here ΔB_{eff} is the effective resolution that the sensor can achieve as a magnetic field measurement is performed. Also, *G* is the applied magnetic field gradient, which is determined by the current in the electromagnets and their geometrical structure. Two major noise sources have been identified in *G*: (1) ∂G_{i}, the error caused by field interpolation; (2) ∂G_{s}, the error caused by variations in supply current[25]. The goal is to keep the contributions by these two error sources below 5% so that the right-hand side in equation (5) reduces to $\approx \Delta B_{\text{eff}}/G$.

Gradient coils' design and assembly

The gradient required along each axis is described by equation (4). Using the coil combinations described in Fig. 3 for the X, Y and Z gradients, monotonically varying magnetic field magnitudes are generated in the FOV[25,48–52]. A single field measurement takes <1 ms. However, to ensure that the ping signal is received by the iMAG device and the measured data are transmitted to the receiver over the Bluetooth protocol, a 50 ms time window is required (Fig. 3e). The 10 ms rise and fall times are due to the L/R time constant of the coils and the switching requirement of the d.c. power supplies. The three gradient coils are assembled using a 50-stranded 32 AWG Litz wire (Fig. 3f). The Z coil consists of two layers, each with 80 turns. Each elongated half of the X and Y coils consists of two layers, with 68 turns per layer. Finally, the three coils are stacked together concentrically to give a single planar structure measuring $60 \times 60 \times 2$ cm^3. For applications requiring a bigger FOV, the physical dimensions can be correspondingly scaled for all the coils. More layers can be added to generate a proportionately higher FOV and/or gradient strength. The d.c. current is another parameter for vertically scaling the FOV. As gradient G increases, the position resolution given in equation (1) improves.

Gradient coil's characterization

The coils in this work were characterized using a setup comprising linear actuators that move in the X, Y and Z directions and by measuring the magnetic field at every 1 cm step (Supplementary Fig. 11). Points between the 1 cm steps are interpolated in MATLAB (R2020a). This results in a finely characterized FOV with steps of 1 mm in X, Y and Z, such that the interpolation error of ∂G_i (equation (5)) causes a <5% variation in G. To reduce the effect of sensor noise from 15 μT_{pp} (measured in the lab) to 1 μT_{pp}, the sensor averages 200 measurements at each location. The Earth's ambient magnetic field is also measured at each location and subtracted from the gradient coil's field. The corrected field values are then stored in the LUT. Each step comprising all the measurements and movement of the actuators takes <15 s, requiring ten days to completely characterize the $40 \times 40 \times 40$ cm^3 FOV with 1 cm increments. The technique for software-based characterization of the coils that requires a much lower time is discussed elsewhere[25]. Also, the entire characterization process needs to be performed only once for a given set of coils, since the magnetic field values for an arbitrary d.c. current can be obtained by linearly scaling the field values stored in the LUT.

Gradient coil's controller board

It is crucial to have a constant d.c. current from the power supply into the coils to minimize ∂G_s in equation (5), which is achieved by designing a controller board. A top-level schematic of the board's circuit is shown in Supplementary Fig. 13. Here V_{REF} and R_1 together set the value of the d.c. current since $I_{d.c.} = V_{REF}/R_1$. An n-channel metal–oxide–semiconductor field-effect transistor driver M_1 (FDL100N50F) rated for 500 V and 100 A is used for handling the high d.c. current coming into the coils. Also, R_1 is chosen with high temperature stability (MP930–0.020–5%) to ensure a thermally stable current value.

Search algorithm

For each measurement, the iMAG first measures the Earth's magnetic field ($\pm$30 to $\pm$60 µT) to cancel its effect from the gradient coil's field. The corrected field values transmitted wirelessly by the iMAG are received by the receiver board and given as an input to the 3D search algorithm implemented in MATLAB, which outputs the corresponding closest position coordinate (Supplementary Fig. 14). The details of the algorithm are described elsewhere[25].

X-gradient variation in FOV

Variation in the X gradient along the Z axis is shown in Fig. 3c. Since the field strength gradually reduces as distance from the surface increases, G_x achieves the highest value of 25.00 mT m^{-1} at $Z = 4$ cm and monotonically reduces to 5.24 mT m^{-1} at $Z = 20$ cm. Variation in the X gradient along the Y axis is shown in Fig. 3d. The circular Z coil results in a field magnitude along the X axis that is non-homogeneous across the Y coordinate. The global coil centre ($Y = 30$ cm) has the highest Z gradient and the highest field magnitude, which gradually falls as Y is increased or decreased[25]. This effect also manifests in the field profile when both X and Z coils are simultaneously powered, where the maximum $G_x = 14.14$ mT m^{-1} occurs at $Y = 32$ cm and falls to 5.65 mT m^{-1} at $Y = 0$ (Fig. 3d).

Communication range study

The communication range between the iMAG and receiver board is evaluated in vitro using different solutions (HCl, NaCl, SGF, SIF and porcine gastric fluid). SGF is prepared as follows: 0.2% w/v NaCl, 0.7% v/v HCl, buffered to a pH of 1.28. The SIF contains more of pancreatin enzyme (composition of lipase, amylase and protease), as opposed to ionic salts and acids (sodium oleate, sodium taurocholate, sodium phosphate and NaCl)[53,54]. For all the tests, a polydimethylsiloxane-encapsulated iMAG is submerged in a cylindrical beaker such that the solution is uniformly distributed around it. The receiver board (nRF52-DK) is kept outside in air and moved as far as possible before losing connection with the iMAG. All the range values beyond 1.0 m are denoted as 1.1 m since the board is not required to be moved farther than 1.0 m under any test scenario. For in vivo tests, the iMAG was placed in the gastric cavity of a pig (Yorkshire swine, 60 kg) with an endoscope (Olympus). The iMAG was held with an endoscopic snare, moved around the stomach to coat it with gastric juice and held in the stomach while communicating with the external receiver.

Communication time study

The communication time and long-term stability of the iMAG were first evaluated under in vitro settings. The iMAG was submerged in an HCl solution (pH 1.5) for two weeks and was communicated with every few hours. The iMAG pill at the end of two weeks was fully functional with no electrical or mechanical damages. This time study was done using HCl to mimic the harsh acidic environment of the stomach as it represents the most extreme case in the entire GI tract. We next performed time studies using other solutions such as SGF, SIF and porcine gastric juice, but those were conducted only for a few days (24–48 h) since the iMAG survived the HCl environment for two weeks.

In vitro testing

During in vitro localization, a $20 \times 20 \times 15\ cm^3$ of saline (9 g NaCl per litre of water) tank is placed on top of the gradient coil's stack (Supplementary Fig. 2). As the iMAG is localized relative to the global origin (0,0,0; Fig. 3a), the error plots (Fig. 3h) show that the error values occur in increments of 1 mm. This is because the LUT (created during characterization) stores field values corresponding to spatial coordinates that are 1 mm apart. For relative localization using another iMAG, the error is computed by subtracting the X, Y and Z components of the decoded distance vector from the ground-truth vector, which results in non-integer values (Fig. 3i) with a peak of <5 mm.

In vivo testing

All the experiments were conducted in accordance with the procedures approved by the Massachusetts Institute of Technology Committee on Animal Care. We chose a swine model due to anatomical similarities of their GI tract to humans as well as their wide usage in GI-tract device evaluation[31]. We observed no adverse effects during the experiments. We administered the iMAG to female Yorkshire swine, 35–65 kg (Tufts). To deliver the iMAG, we placed the swine on a liquid diet 24 h before the procedure and fasted the swine overnight. We sedated them with an intramuscular injection of Telazol (tiletamine/zolazepam) (5.00 mg kg^{-1}), xylazine (2.00 mg kg^{-1}) and atropine (0.05 mg kg^{-1}), as well as supplemental isoflurane (1–3% in oxygen), if needed, via a face mask. An orogastric tube or overtube was placed with the guidance of a gastric endoscope and remained in the oesophagus to ease the passage of the device. In the first experiment, two iMAG devices at a known distance apart were passed through the overtube and placed into the insufflated stomach (Fig. 4b–e). Although the swine were fasted, some of them still possessed food in their stomach during iMAG delivery. In the second experiment, an iMAG was inserted into the insufflated stomach through the overtube and left to pass through the GI tract (Fig. 4f–p). Magnetic field measurements were made in the chute followed by an X-ray scan to determine residency time of the devices as well as for any evidence of GI perforation (pneumoperitoneum). This was repeated on all the subsequent test days (Monday/Wednesday/Friday) until the ingested iMAG was excreted. Additionally, during the retention of devices, the animals were clinically evaluated for normal feeding and stooling patterns. No evidence of pneumoperitoneum on X-ray nor any changes in feeding or stooling patterns were observed. In the third experiment, to validate our FI model (Fig. 5a–c), an iMAG was tethered on the tip of a catheter and placed into the rectum. The iMAG's location was repeatedly scanned (using both magnetic field measurements and X-rays) as the device was gradually pulled out in 1–2 cm increments. Similar steps were executed during the final experiment to examine the potential interference caused by magnetic materials surrounding the iMAG (Fig. 5d–i), with magnetic beads placed in the rectum before iMAG's insertion.
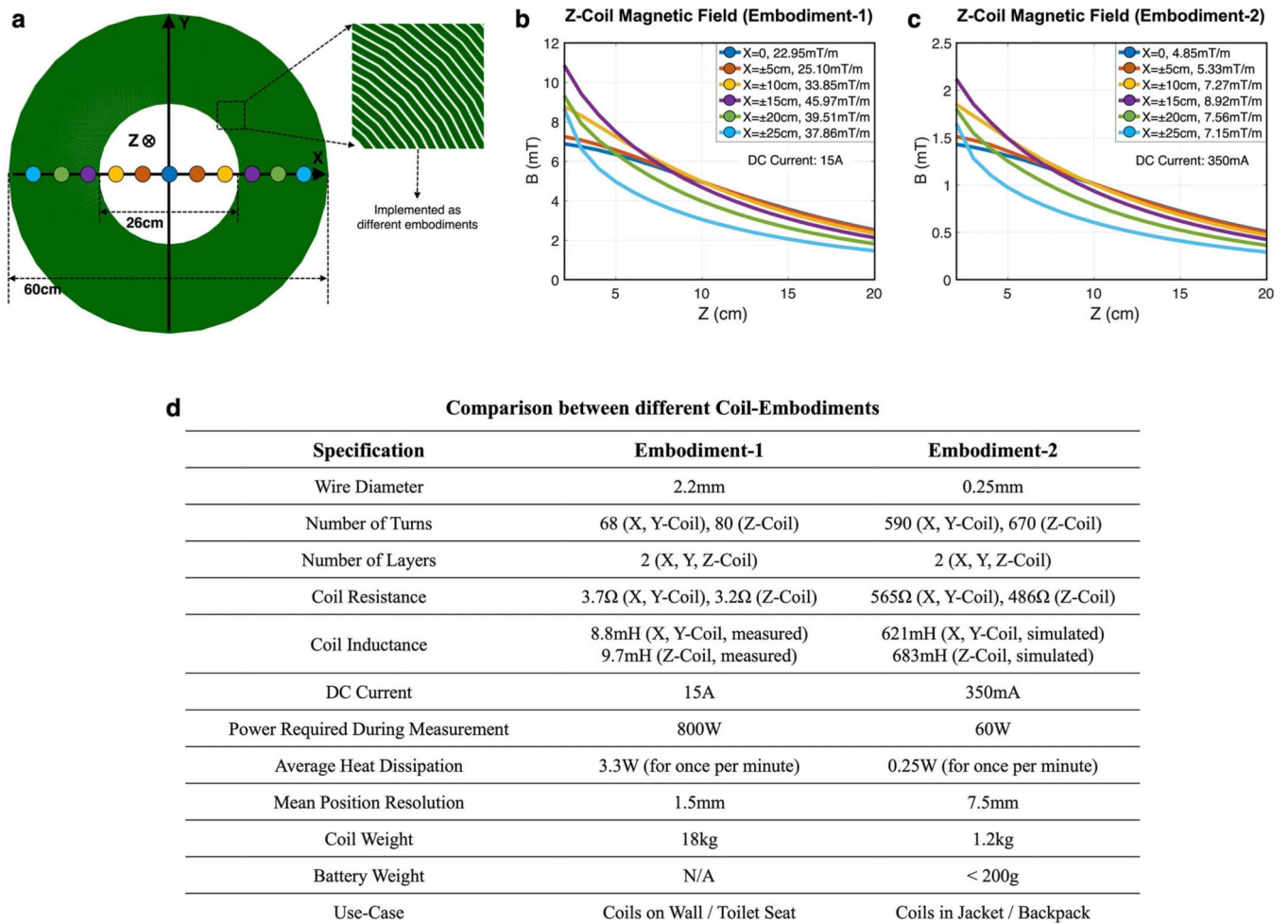
During all the in vivo tests, the receiver board was kept close to the animal's abdominal region and connected to a computer displaying the received magnetic field values from the iMAG devices. Animals also had a reference iMAG secured on the skin using a Tegaderm patch. After performing magnetic field measurements in the chute (Fig. 4a), the animal was physically carried to the X-ray scanner every time a scan was required. During this motion, it was hard to keep the position of the iMAGs intact due to the relative movement

of the animal's organs. Additionally, to get two orthogonal X-ray scans to compute the 3D interdevice distance, the animal was manually rotated by 90°, which does not result in perfect orthogonality. Therefore, comparisons with X-ray scans show a difference of >5 mm for localization in the colon (Fig. 4m,n), which is an artefact resulting from the X-ray acquisition methodology.

Software

J-Link RTT Viewer (V6.62a) was used for collecting the raw magnetic field values from the iMAG pills and nRF receiver. MATLAB (R2020a) was used for position decoding using the field values. Arduino Mega 2560 and Arduino IDE (1.8.19) were used for FOV characterization and LUT creation, respectively. MATLAB (R2020a) and GraphPad Prism (9.4.1) were used for data analysis and plotting. Illustrations were made in Adobe Illustrator (26.4.1) and Microsoft PowerPoint (16.69.1).
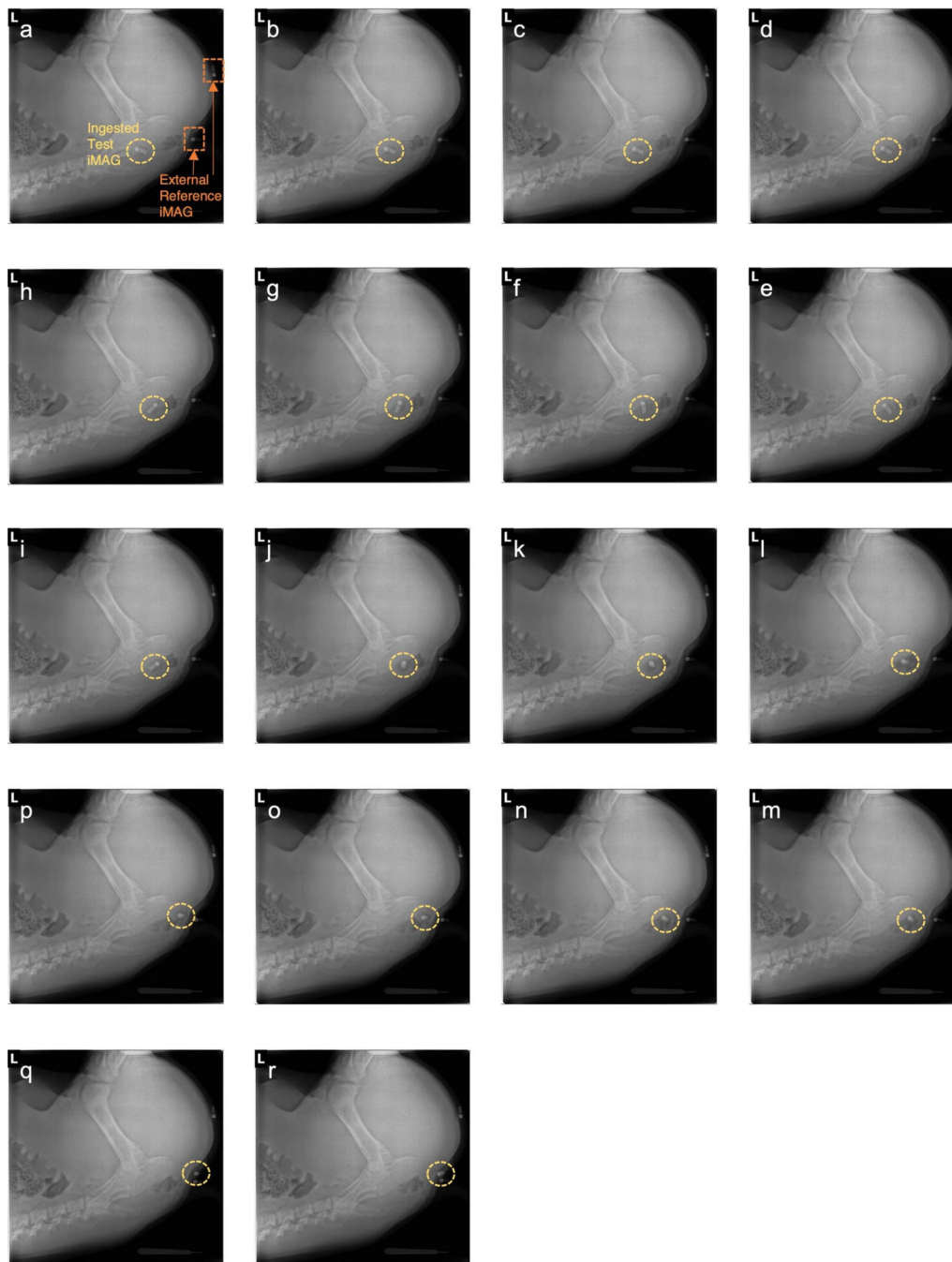
Extended Data

Comparison between different Coil-Embodiments

Specification	Embodiment-1	Embodiment-2
Wire Diameter	2.2mm	0.25mm
Number of Turns	68 (X, Y-Coil), 80 (Z-Coil)	590 (X, Y-Coil), 670 (Z-Coil)
Number of Layers	2 (X, Y, Z-Coil)	2 (X, Y, Z-Coil)
Coil Resistance	3.7Ω (X, Y-Coil), 3.2Ω (Z-Coil)	565Ω (X, Y-Coil), 486Ω (Z-Coil)
Coil Inductance	8.8mH (X, Y-Coil, measured) 9.7mH (Z-Coil, measured)	621mH (X, Y-Coil, simulated) 683mH (Z-Coil, simulated)
DC Current	15A	350mA
Power Required During Measurement	800W	60W
Average Heat Dissipation	3.3W (for once per minute)	0.25W (for once per minute)
Mean Position Resolution	1.5mm	7.5mm
Coil Weight	18kg	1.2kg
Battery Weight	N/A	< 200g
Use-Case	Coils on Wall / Toilet Seat	Coils in Jacket / Backpack

Extended data Extended Data Fig. 1. Coil embodiments for different use-cases.

a, The flat-spiral Z-coil is shown and is made using several loops of copper wire beginning from an inner diameter of 26 cm and extending to an outer diameter of 60 cm. Using different diameters of the copper wire, different embodiments of the Z-coil (and similarly the X and Y coils) can be realized. **b**, Gradient profiles generated by the Z-coil of Embodiment-1 carrying 15 A of d.c. current. The prototype used in this work is an implementation of Embodiment-1. **c**, Gradient profiles generated by the Z-coil of Embodiment-2 carrying 350 mA of d.c. current. The gradient in Embodiment-2 is only 5x lower than the gradient in Embodiment-1, while the d.c. current is 43x lower. **d**, This is achieved by using a much smaller diameter of the copper wire for Embodiment-2 that results in ≈9x increase in the number of turns that can be fitted in the same coil footprint. The 350 mA of current leads to only 0.25 W of heat (corresponding to <0.1 °C increase in the surface temperature of the coils) for a measurement done every minute, which is sufficient for monitoring the GI transit-time and motility. For applications requiring a higher sampling rate (maximum achievable 3.3 Hz by the current system), thermal insulators can be used around the coils to alleviate the heating. The 7.5 mm of mean position resolution for Embodiment-2 is acceptable for localization in the GI tract. The total weight of the coils in Embodiment-2 and the required battery for powering the coils is suitable for portable prototypes such as jackets or backpacks.
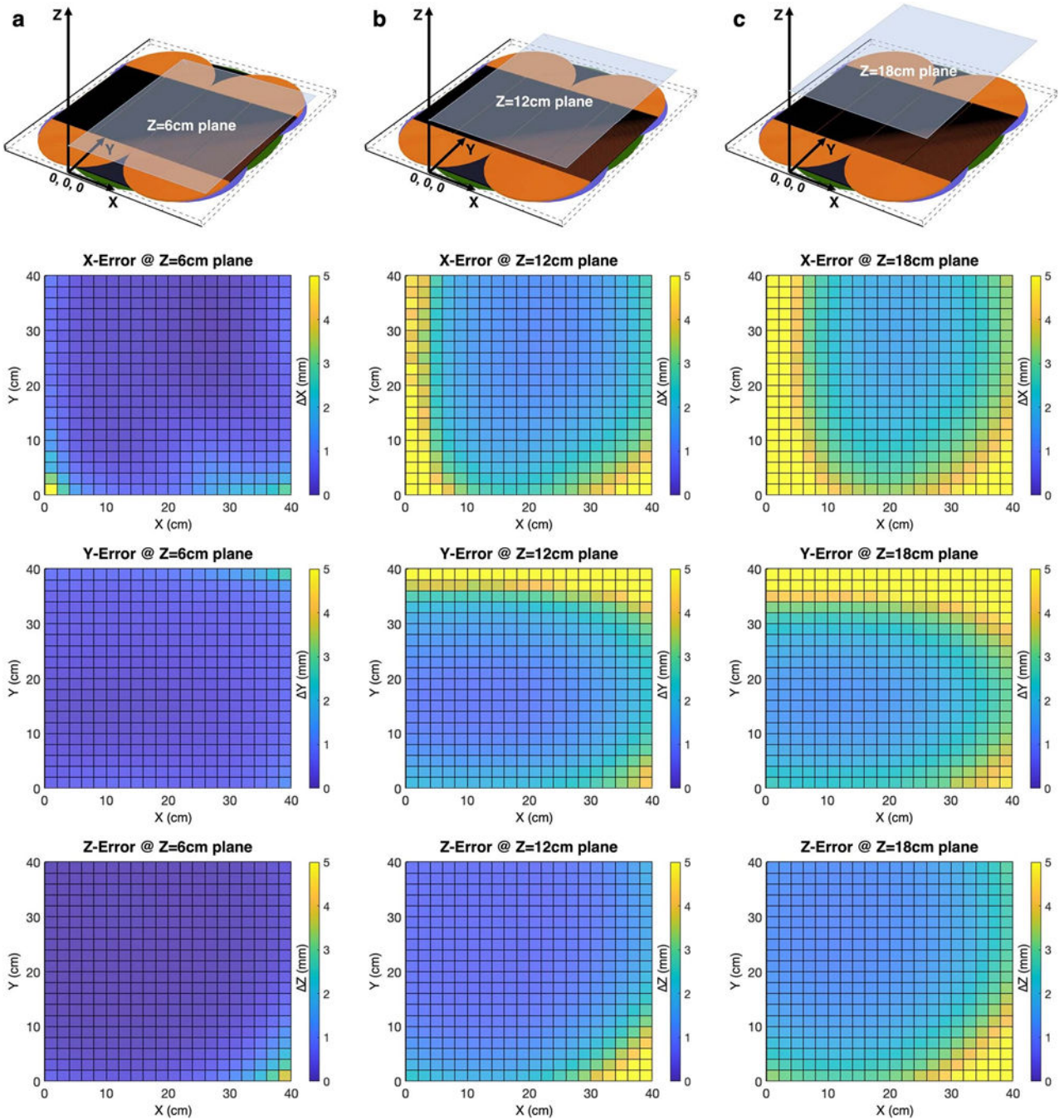
Extended Data Fig. 2. Localization error of iMAG as a function of distance from the coils

a, The spatial error while localizing a single iMAG relative to the gradient coils is plotted for Z = 6 cm plane. The X, Y and Z errors (shown below the coil-setup) are close to the lower error-bound of the system (≈1 mm). **b**, The spatial errors are plotted for Z = 12 cm plane and the errors in most regions of the FOV are in 1–2 mm range. The transition to the higher error-bound of the system (≈5 mm) is visible at the boundary panes of the FOV. **c**, The spatial errors are plotted for Z = 18 cm plane and the presence of the higher error-bound of the system (yellow regions) is more prominent at the boundary planes of the

FOV compared to the Z = 12 cm plane. The FOV ends at Z = 20 cm and the remaining half of the 40x40x40cm3 FOV is covered by the other set of the gradient coils shown in Fig. 4a.


Extended Data Fig. 3. X-Ray scans for fecal incontinence study.
a-r, Consecutive X-ray scans obtained while moving the iMAG (connected to a catheter) out of the anal sphincter in steps of five mm during the fecal incontinence study. Detailed results shown in Fig. 5a–c.
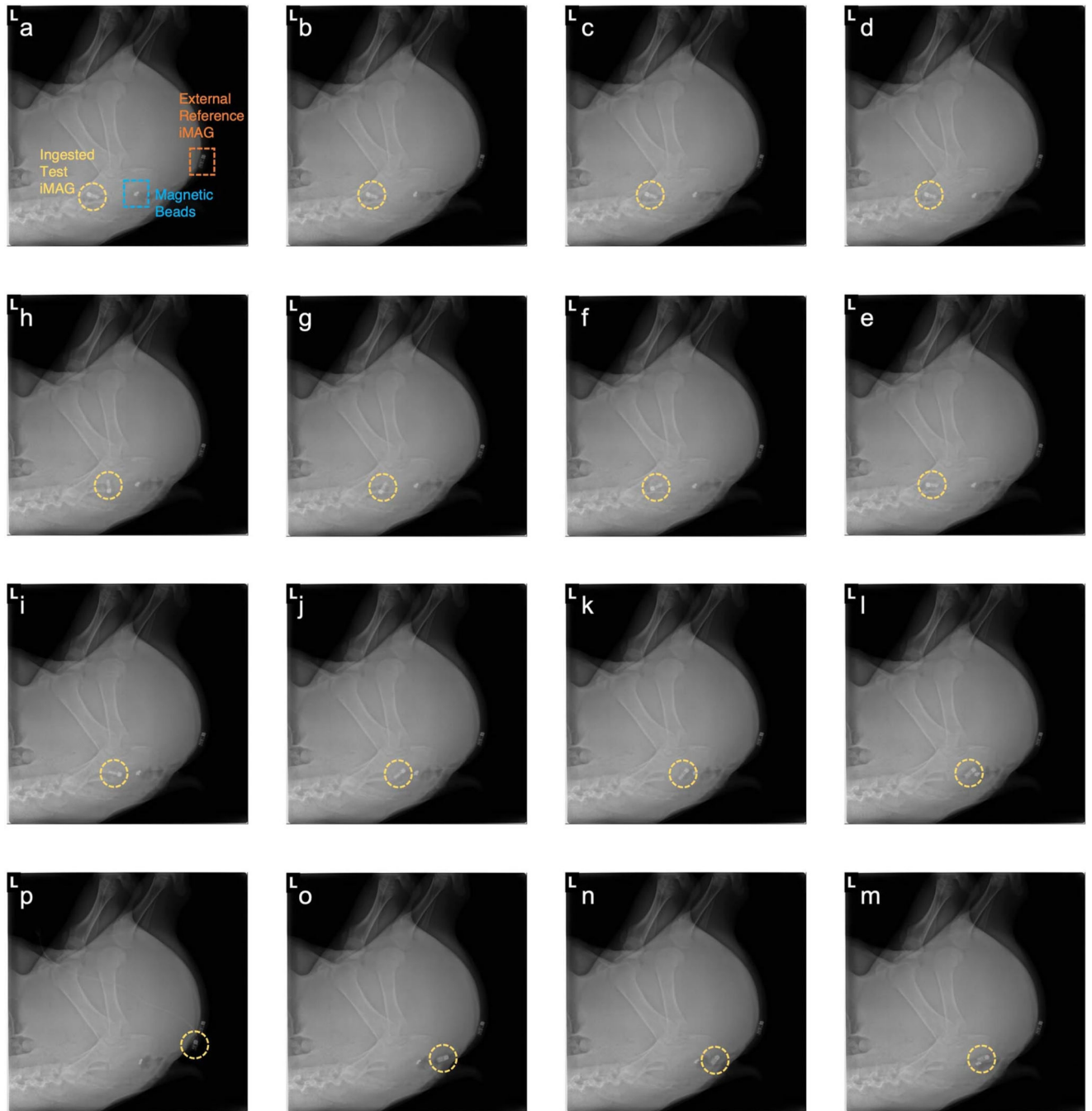
Extended Data Fig. 4. X-ray scans for magnetic label tracking.
a-p, Consecutive X-ray scans obtained while moving the iMAG (connected to a catheter) out of the anal sphincter in steps of five mm during the magnetic label (barium beads) tracking study. Detailed results shown in Fig. 5d–i.
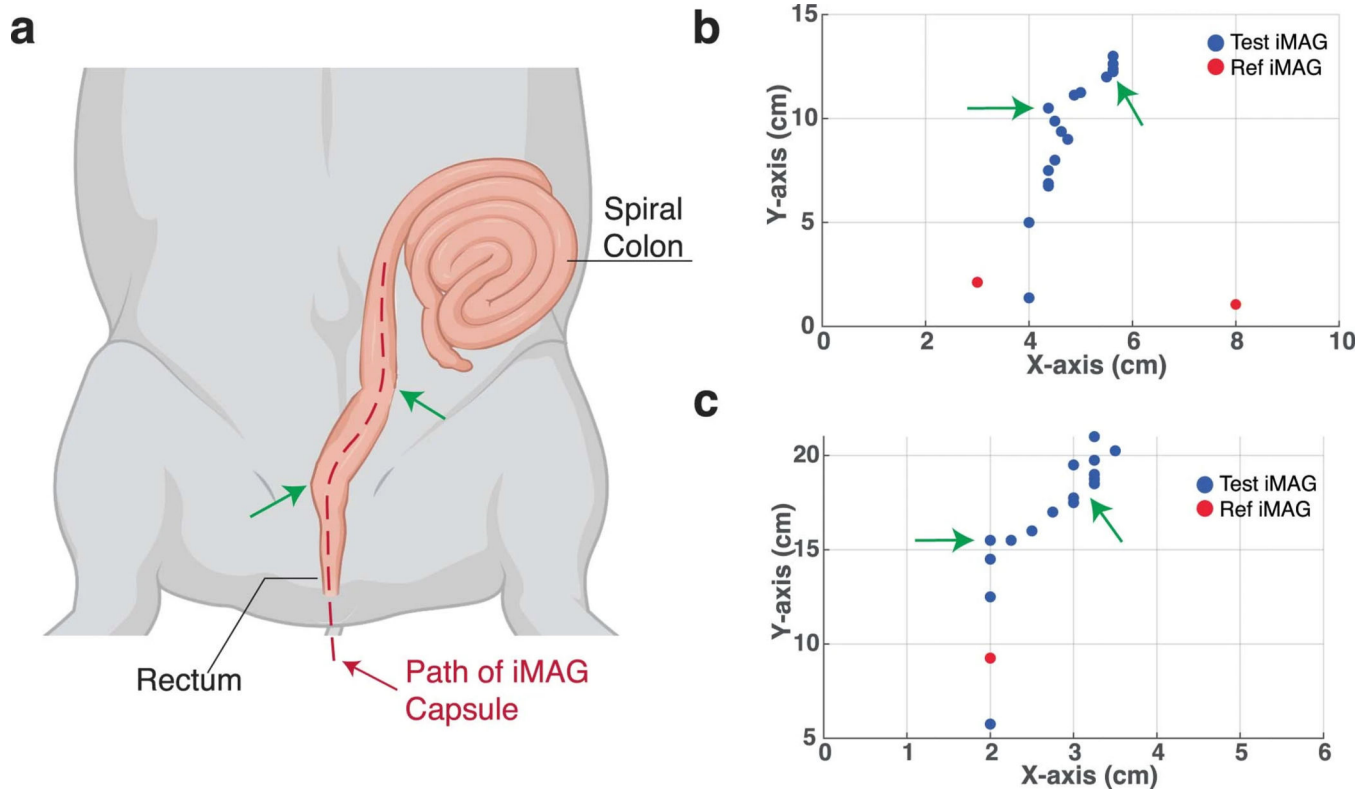
Extended Data Fig. 5. iMAG trajectory compared to the meanders in colon.
a, Pig's colon shown for comparison. **b**, iMAG trajectory from the fecal incontinence monitoring study. **c**, iMAG trajectory from the magnetic label tracking study. The two sharp bends in the rectum are prominently visible (highlighted by green arrows) in (**a**) and are captured by both the iMAG trajectories shown in (**b**) and (**c**). This shows that our technology can distinguish anatomical features for organs that are retroperitoneally fixed in the GI tract, like colon. The trajectory maps in (**b**) and (**c**) are created by plotting together all the decoded position coordinates of iMAG using the magnetic field measurements performed by it as it moves along the colon.
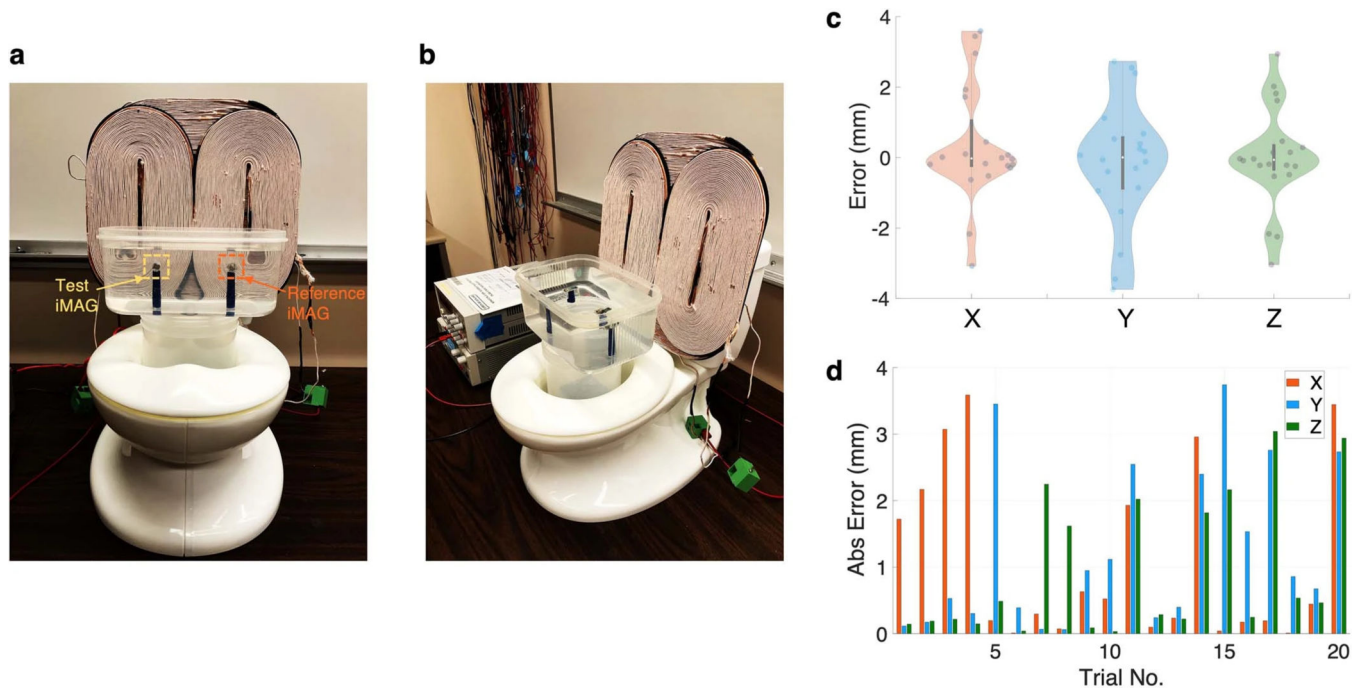
Extended Data Fig. 6. iMAG for smart toilets.
a, Front-view of the gradient coils assembly mounted on a toilet seat for continuous GI monitoring. **b**, Side-view of the toilet seat with the gradient coils. Two iMAG devices are placed in a tank filled with saline solution to demonstrate 3D localization. The experiment is repeated for n = 20 different locations of the iMAG devices in the FOV. **c**, Error obtained at all the locations is clustered together and plotted. **d**, Error at each location is plotted separately. Error reported as mean ± s.d.: 1.09 ± 1.29 mm (X), 1.25 ± 1.22 mm (Y), 0.95 ± 1.05 mm (Z). This prototype shows the ability of our technology to be deployed in common human-specific settings.

Supplementary Material

Refer to Web version on PubMed Central for supplementary material.

Acknowledgements

Data availability

The data that support the findings of this study are available from the corresponding authors upon reasonable request.

References

1. Steiger C. et al. Ingestible electronics for diagnostics and therapy. Nat. Rev. Mater 4, 83–98 (2019).

2. Keller J. et al. Advances in the diagnosis and classification of gastric and intestinal motility disorders. Nat. Rev. Gastroenterol. Hepatol 15, 291–308 (2018). [PubMed: 29622808]

3. Rao SSC et al. Evaluation of gastrointestinal transit in clinical practice: position paper of the American and European Neurogastroenterology and Motility Societies. Neurogastroenterol. Motil 23, 8–23 (2011). [PubMed: 21138500]

4. Mimee M. et al. An ingestible bacterial-electronic system to monitor gastrointestinal health. Science 360, 915–918 (2018). [PubMed: 29798884]

5. Kuo B. et al. Comparison of gastric emptying of a nondigestible capsule to a radio-labelled meal in healthy and gastroparetic subjects. Aliment. Pharmacol. Ther 27, 186–196 (2008). [PubMed: 17973643]

6. Wang A. et al. Wireless capsule endoscopy. Gastrointest. Endosc 78, 805–815 (2013). [PubMed: 24119509]

7. Hejazi RA et al. Video capsule endoscopy: a tool for the assessment of small bowel transit time. Front. Med 3, 6 (2016).

8. Maqbool S. et al. Wireless capsule motility: comparison of the SmartPill GI monitoring system with scintigraphy for measuring whole gut transit. Digestive Dis. Sci 54, 2167–2174 (2009).

9. Dagdeviren C. et al. Flexible piezoelectric devices for gastrointestinal motility sensing. Nat. Biomed. Eng 1, 807–817 (2017). [PubMed: 31015594]

10. Haase AM et al. Gastrointestinal motility during sleep assessed by tracking of telemetric capsules combined with polysomnography—a pilot study. Clin. Exp. Gastroenterol 8, 327–332 (2015). [PubMed: 26677340]

11. Gharibans AA et al. Artifact rejection methodology enables continuous, noninvasive measurement of gastric myoelectric activity in ambulatory subjects. Sci. Rep 8, 5019 (2018). [PubMed: 29568042]

12. Chen H. et al. Advances in functional X-ray imaging tec hniques and contrast agents. Phys. Chem. Chem. Phys 14, 13469–13486 (2012). [PubMed: 22962667]

13. Monge M. et al. Localization of microscale devices in vivo using addressable transmitters operated as magnetic spins. Nat. Biomed. Eng 1, 736–744 (2017). [PubMed: 31015668]

14. Worsøe J. et al. Gastric transit and small intestinal transit time and motility assessed by a magnet tracking system. BMC Gastroenterol. 11, 145 (2011). [PubMed: 22206545]

15. Andrä W. et al. A novel method for real-time magnetic marker monitoring in the gastrointestinal tract. Phys. Med. Biol 45, 3081–3093 (2000). [PubMed: 11049189]

16. Son D. et al. A 5-D localization method for a magnetically manipulated untethered robot using a 2-D array of Hall-effect sensors. IEEE/ASME Trans. Mechatron 21, 708–716 (2016). [PubMed: 27458327]

17. Pourhomayoun M. et al. Accurate localization of in-body medical implants based on spatial sparsity. IEEE Trans. Biomed. Eng 61, 590–597 (2014). [PubMed: 24108709]

18. Weitschies W. et al. Magnetic marker monitoring: high resolution real-time tracking of oral solid dosage forms in the gastrointestinal tract. Eur. J. Pharm. Biopharm 74, 93–101 (2010). [PubMed: 19619649]

19. Franz AM et al. Electromagnetic tracking in medicine—a review of technology, validation, and applications. IEEE Trans. Med. Imaging 33, 1702–1725 (2014). [PubMed: 24816547]

20. Brink CE et al. Magnetic tracking of gastrointestinal motility. Physiol. Meas 41, 12TR01 (2020).

21. Baker-Jarvis J. & Kim Sung The interaction of radio-frequency fields with dielectric materials at macroscopic to mesoscopic scales. J. Res. Natl Inst. Stand. Technol 117, 1–60 (2012). [PubMed: 26900513]

22. Schiller C. et al. Intestinal fluid volumes and transit of dosage forms as assessed by magnetic resonance imaging. Aliment. Pharmacol. Ther 22, 971–979 (2005). [PubMed: 16268972]

23. Mudie DM et al. Physiological parameters for oral delivery and in vitro testing. Mol. Pharmaceutics 7, 1388–1405 (2010).

24. Dove I. Analysis of radio propagation inside the human body for in-body localization purposes. Thesis, University of Twente (2014).

25. Sharma S. et al. Wireless 3D surgical navigation and tracking system with 100μm accuracy using magnetic-field gradient-based localization. IEEE Trans. Med. Imaging 40, 2066–2079 (2021). [PubMed: 33819153]

26. Ham CLG et al. Peripheral nerve stimulation during MRI: effects of high gradient amplitudes and switching rates. J. Magn. Reson. Imaging 7, 933–937 (1997). [PubMed: 9307922]

27. Schaefer DJ et al. Review of patient safety in time- varying gradient fields. J. Magn. Reson. Imaging 20, 20–29 (2000).

28. Klein V. et al. Investigating cardiac stimulation limits of MRI gradient coils using electromagnetic and electrophysiological simulations in human and canine body models. Magn. Reson. Med 85, 1047–1061 (2021). [PubMed: 32812280]

29. Sharma S. et al. 20.4 3D surgical alignment with 100μm resolution using magnetic-field gradient-based localization. In Proc. 2020 IEEE International Solid-State Circuits Conference— (ISSCC) 318–320 (IEEE, 2020).

30. Mostafaei F. et al. Variations of MRI-assessed peristaltic motions during radiation therapy. PLoS ONE 13, e0205917 (2018).

31. Swindle MM et al. Swine as models in biomedical research and toxicology testing. Vet. Pathol 49, 344–356 (2012). [PubMed: 21441112]

32. Ruiz NS et al. Fecal incontinence—challenges and solutions. World J. Gastroenterol 23, 11–24 (2017). [PubMed: 28104977]

33. Lo YK et al. A wireless implant for gastrointestinal motility disorders. Micromachines 9, 17 (2018). [PubMed: 30393295]

34. Kong YL et al. 3D-printed gastric resident electronics. Adv. Mater. Technol 4, 1800490 (2019).

35. Ramadi KB, Srinivasan SS & Traverso G. Electroceuticals in the gastrointestinal tract. Trends Pharmacol. Sci 41, 960–976 (2020). [PubMed: 33127099]

36. Traverso G. et al. Physiologic status monitoring via the gastrointestinal tract. PLoS ONE 10, e0141666 (2015).

37. Menciassi A. et al. Clamping tools of a capsule for monitoring the gastrointestinal tract problem analysis and preliminary technological activity. In Proc. 2005 IEEE International Conference on Robotics and Automation 1309–1314 (IEEE, 2005).

38. Than TD et al. A review of localization systems for robotic endoscopic capsules. IEEE Trans. Biomed. Eng 59, 2387–2399 (2012). [PubMed: 22736628]

39. Su S. et al. Investigation of the relationship between tracking accuracy and tracking distance of a novel magnetic tracking system. IEEE Sens. J 17, 4928–4937 (2017).

40. Bianchi F. et al. Localization strategies for robotic endoscopic capsules: a review. Expert Rev. Med. Devices 16, 381–403 (2019). [PubMed: 31056968]

41. Pham DM et al. A real-time localization system for an endoscopic capsule using magnetic sensors. Sensors 14, 20910–20929 (2014). [PubMed: 25379813]

42. Bass DM et al. Gastrointestinal safety of an extended-release, nondeformable, oral dosage form (OROS$^{®}$)1. Drug-Saf. 25, 1021–1033 (2002). [PubMed: 12408733]

43. Huang J. et al. IM6D: magnetic tracking system with 6-DOF passive markers for dexterous 3D interaction and motion. ACM Trans. Graph 34, 217 (2015).

44. Vasisht D. et al. In-body backscatter communication and localization. In Proc. 2018 Conference of the ACM Special Interest Group on Data Communication 132–146 (ACM, 2018).

45. Nadeau P. et al. Prolonged energy harvesting for ingestible devices. Nat. Biomed. Eng 1, 0022 (2017). [PubMed: 28458955]

46. Talkhooncheh AH et al. A fully-integrated biofuel-cell-based energy harvester with 86% peak efficiency and 0.25V minimum input voltage using source-adaptive MPPT. In 2020 IEEE Custom Integrated Circuits Conference (CICC) 1–4 (IEEE, 2020).

47. Talkhooncheh AH et al. A biofuel-cell-based energy harvester with 86% peak efficiency and 0.25-V minimum input voltage using source-adaptive MPPT. IEEE J. Solid-State Circuits 56, 715–728 (2021).

48. Turner R. Gradient coil design: a review of methods. Magn. Reson. Imaging 11, 903–920 (1993). [PubMed: 8231676]

49. Hidalgo-Tobon SS Theory of gradient coil design methods for magnetic resonance imaging. Concepts Magn. Reson 36A, 223–242 (2010).

50. Sharma S. et al. Electromagnet gradient coil apparatus for micro-device localization. US patent 11,457,835 B2 (2021).

51. Sharma S. et al. In-vivo monitoring of an internal volume of a mammal using magnetic field gradients. US patent 20,210,137,412 (2021).

52. Sharma S. et al. Surgical alignment by magnetic field gradient localization. US patent 11,399,848 B2 (2019).

53. Khadra I. et al. Statistical investigation of simulated intestinal fluid composition on the equilibrium solubility of biopharmaceutics classification system class II drugs. Eur. J. Pharm. Sci 25, 65–75 (2015).

54. Vertzoni M. et al. Dissolution media simulating the intralumenal composition of the small intestine: physiological issues and practical aspects. J. Pharm. Pharmacol 56, 453–462 (2004). [PubMed: 15099440]

55. Nevo E. et al. Method and apparatus to estimate location and orientation of objects during magnetic resonance imaging. US patent 6,516,213 B1 (2003).
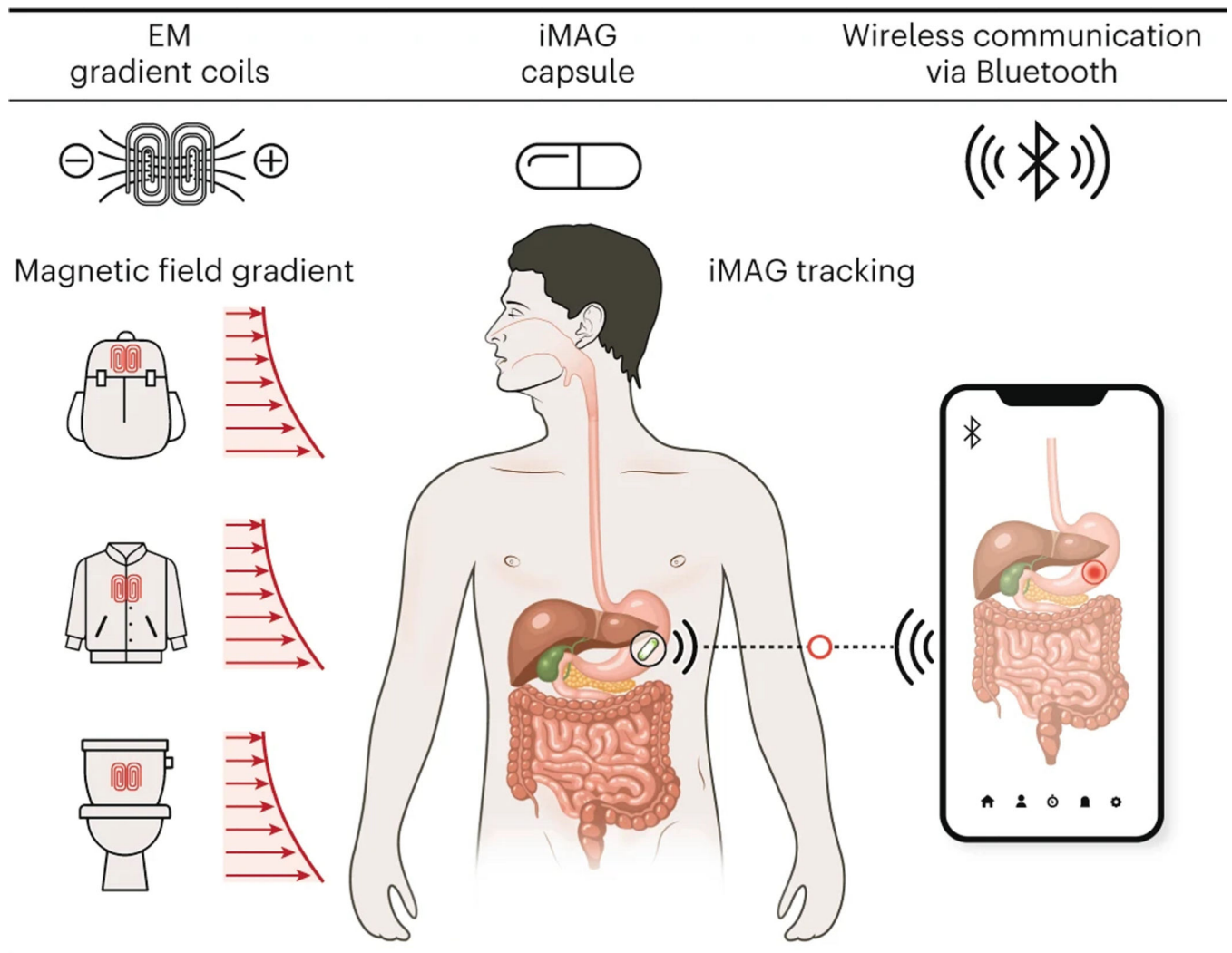
Fig. 1 |. System overview.
Overview of the complete magnetic-field-gradient-based tracking system is shown. A wireless iMAG is shown inside the patient. An external smartphone/receiver sends a wireless ping signal to the iMAG to measure its local magnetic field. The measured field value is transmitted by the iMAG to the receiver, which maps it to the corresponding spatial coordinates and displays the 3D location in real time. The magnetic field is generated by planar EM coils placed behind the patient's back, which can be customized to form a wearable jacket, put into a backpack with batteries or attached to a toilet seat for continuous GI tract monitoring. The field generated by the electromagnets is strictly monotonic in nature, resulting in a magnetic field gradient that uniquely encodes each spatial point.
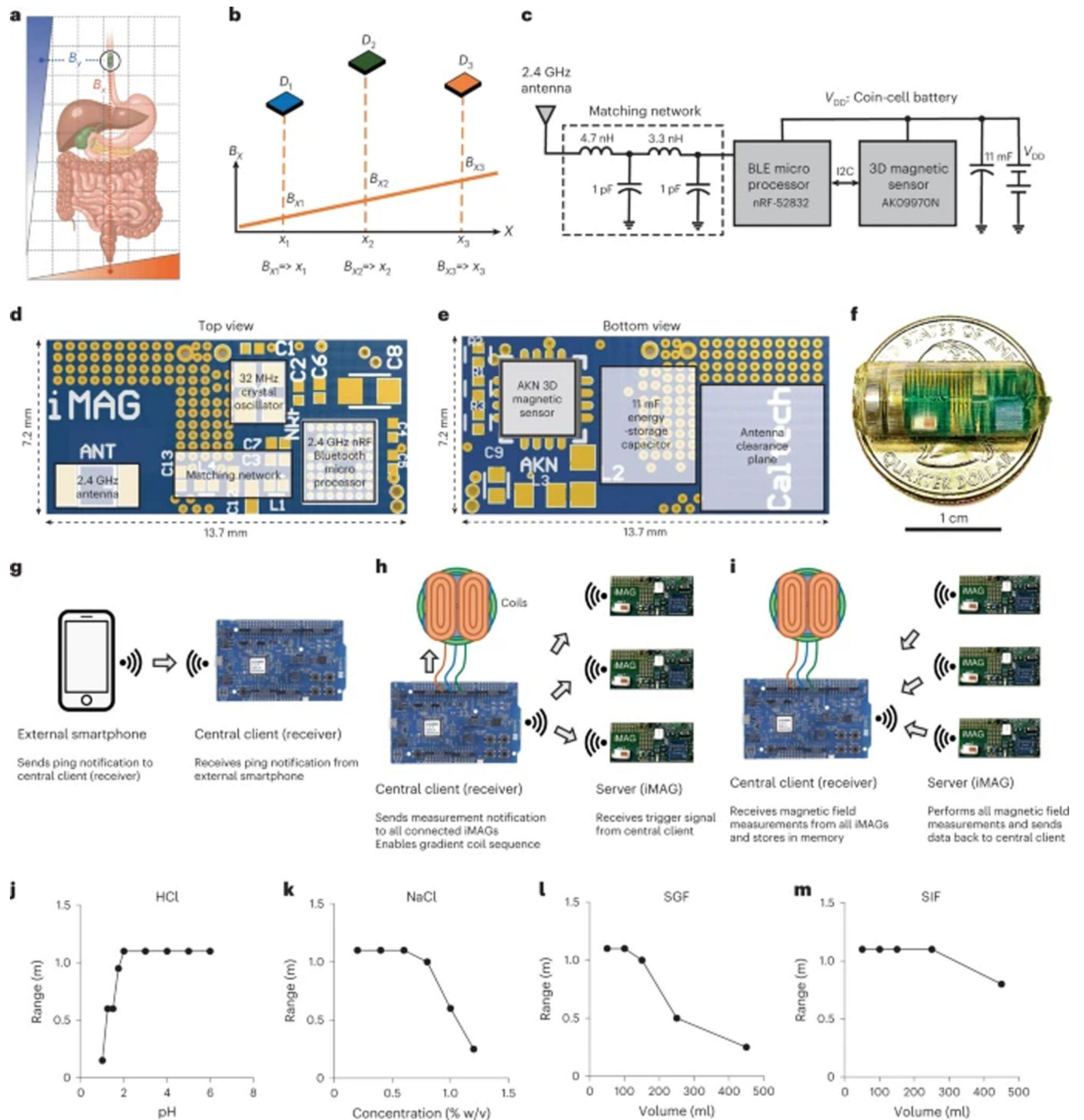
Fig. 2 |. iMAG device architecture and characterization.
a, The iMAG device is shown inside the patient's GI tract with magnetic field gradients present along the three axes (shown only along the *X* and *Y* axes for simplicity). **b**, Conceptual overview of the 3D localization of magnetic sensing devices D_1-D_3. A monotonically varying magnetic field is generated to result in a field gradient along the *X* axis. Each device measures the total field magnitude at its location, which is unique for each point along the *X* axis, thereby allowing oneto-one mapping from field to position. This process is repeated for localization along the *Y* and *Z* axes. **c**, The iMAG consists of

a 3D magnetic sensor, a BLE microprocessor to communicate with the sensor, an antenna to communicate with the external receiver and coin-cell batteries for power. **d,e**, Top (**d**) and bottom (**e**) views of the iMAG PCB showing the placement of critical circuit blocks. **f**, The iMAG is encapsulated to form a cylindrical pill measuring 20 mm in length and 8 mm in diameter. **g–i**, Complete communication protocol between the smartphone, receiver board, iMAG devices and gradient coils is illustrated. **j–m**, In vitro characterization of the communication range between the iMAG and receiver board. The range was measured for 250 ml HCl with varying pH (**j**), 500 ml NaCl solution with varying salt concentrations (**k**), SGF (**l**) and SIF (**m**) with varying quantities. All the range values greater than 1.0 m are labelled as 1.1 m since that is the sufficient range here.
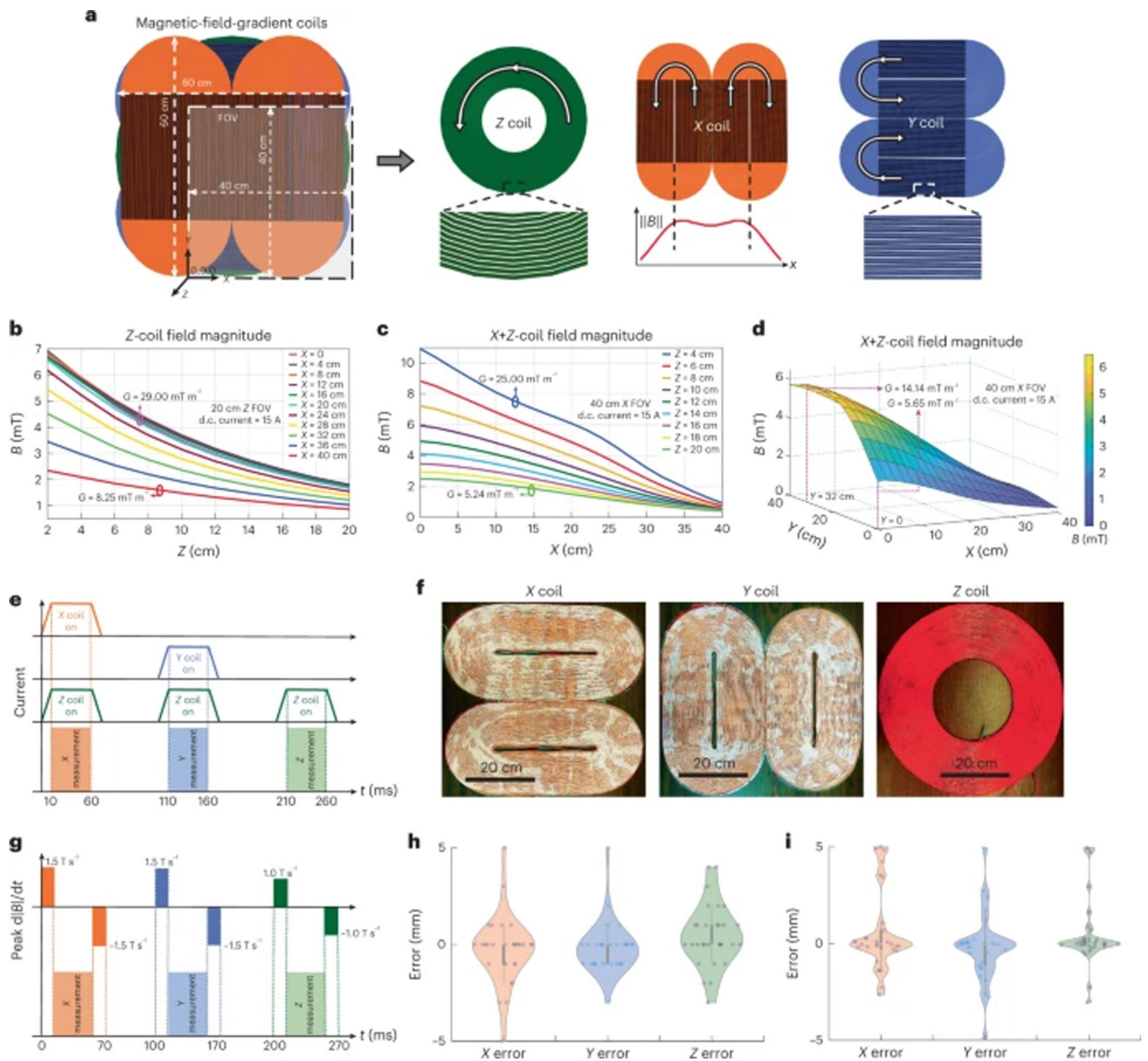
Fig. 3 |. Magnetic-field-gradient generation and characterization.

a, Magnetic-field-gradient-generating coils for *X*, *Y* and *Z* are shown. The *Z* coil consists of a single spiral carrying current in one direction. The *X* coil consists of two elongated spirals carrying currents in opposite directions. The magnitude function causes both spirals to produce identical field values. The *Y* coil is identical and orthogonal to *X*. All three coils are stacked together concentrically, resulting in a planar coil structure with an effective FOV of $40 \times 40 \times 20$ cm^3. **b**, Magnetic field profile produced by the *Z* coil, plotted along the *Z* axis as the *X* coordinate is varied (at *Y* = 20 cm). Identical plots are obtained as the *Y* coordinate is varied since the field is symmetric about the *X* and *Y* directions. **c**, *X*-axis magnetic field profile, plotted for varying *Z* coordinates (at *Y* = 20 cm), when both *X* and *Z* coils are on

together. **d**, X-axis field profile as the Y coordinate is varied (at $Z = 10$ cm). Similar plots are obtained along the Y axis when both Y and Z coils are on together. **e**, Global timing diagram showing the measurement phases with the on/off times of the gradient coils. The Z coil is kept on during the X and Y measurements to produce monotonically varying magnetic field magnitudes along the respective axes. **f**, Fully assembled X, Y and Z gradient coils using 50/32 AWG Litz wire. **g**, Peak $d|B|/dt$ values plotted for the entire measurement phase. All the values are considerably lower than the recommended safety threshold of 20 T s^{-1}. **h**, Error in the decoded position of a single iMAG localized with respect to the global origin (0,0,0 on the coils) at $n = 30$ different locations chosen uniformly in the FOV. The error as mean ± standard deviation (s.d.): $1.07 ± 1.44$ mm (X), $0.77 ± 1.07$ mm (Y), $1.13 ± 1.20$ mm (Z). **i**, Error in the decoded position of an iMAG localized with respect to another iMAG at a known location serving as a relative reference, eliminating the need for a global reference. Here $n = 30$ different locations were uniformly chosen in the FOV. Error as mean ± s.d.: $1.34 ± 1.68$ mm (X), $1.13 ± 1.38$ mm (Y), $0.97 ± 1.55$ mm (Z).
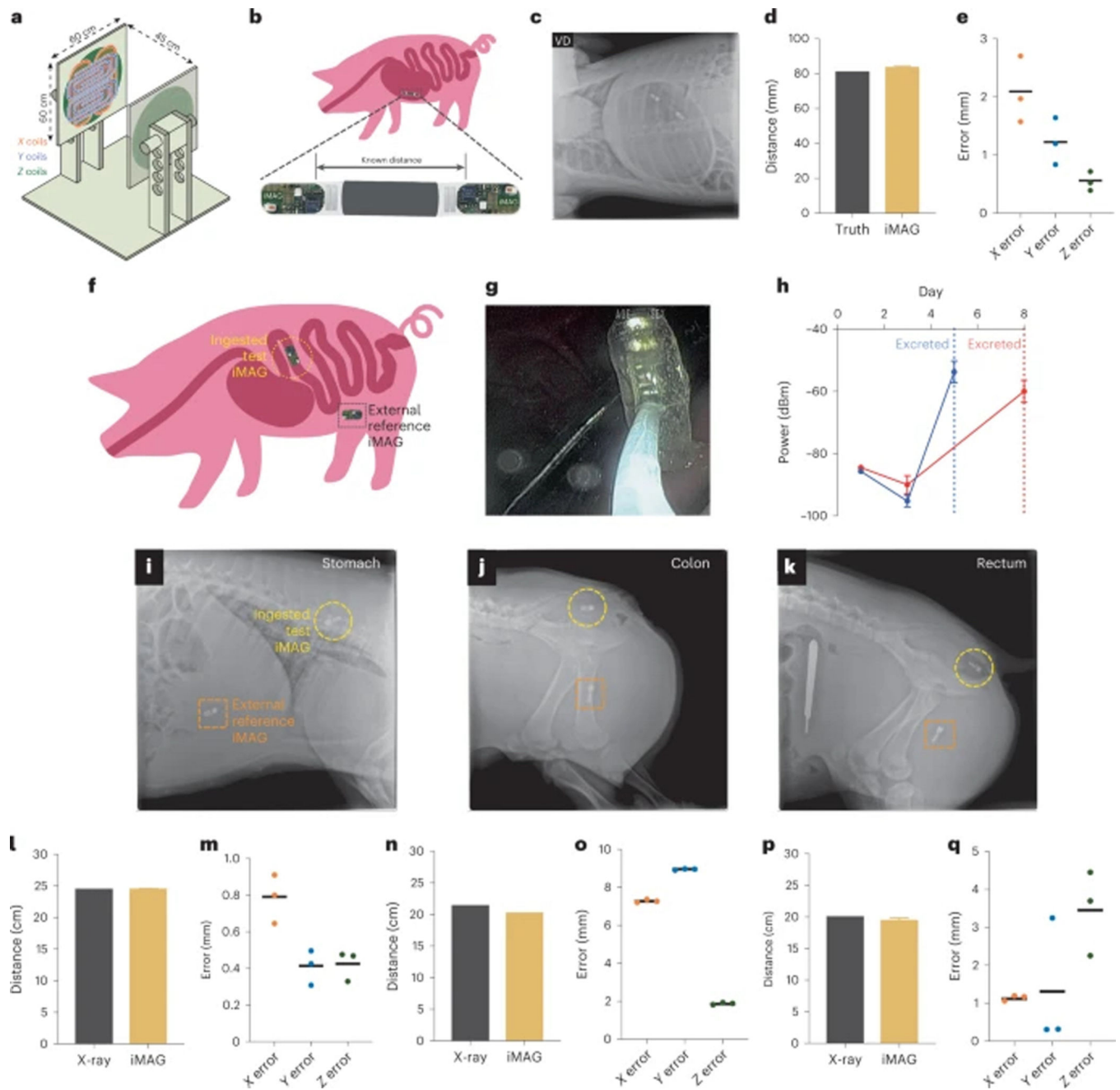
Fig. 4 |. In vivo localization of iMAG in the GI tract under acute and chronic conditions.
a, Custom-designed wooden chute with two sets of gradient coils on each side to provide
a $40 \times 40 \times 40$ cm^3 FOV with adjustable height. **b**, Test fixture with two iMAG devices
positioned a fixed distance apart and lodged into the gastric cavity of the pig. **c**, X-ray scan
of the animal showing the position of the test fixture. **d**, Decoded interdevice distance from
the iMAG is 83.60 ± 0.70 mm (mean $\pm$ s.d.), plotted alongside the ground-truth distance
of 81.12 mm. **e**, Individual errors in the X, Y and Z components of the decoded distance
are plotted. **f**, For chronic studies, two iMAG devices are used, with one serving as the
ingested test iMAG and the other attached externally on the skin in the abdominal region

to serve as the reference iMAG. Localization of the two devices is performed on each test day (Monday/Wednesday/Friday). **g**, To avoid the animal chewing on the test iMAG, it is endoscopically administered. **h**, Signal strength (plotted as mean ± s.d.) detected by the receiver as the ingested iMAG is localized on different test days. When located in the stomach and SI, the signal strength is –80 to –100 dBm, which increases to –70 dBm or higher when located in the colon or rectum. **i–k**, To compare the decoded distance of the ingested iMAG with the reference, X-ray scans were conducted when the iMAG was located in the stomach (**i**), colon (**j**) and rectum (**k**). Position of the external reference iMAG is shown in each scan. **l–q**, The error between the distance given by the X-ray and iMAG is found to be (reported as mean ± s.d.) 0.54 ± 0.21 mm for the stomach (**l** and **m**), 6.04 ± 3.70 mm for the colon (**n** and **o**) and 1.97 ± 1.30 mm for the rectum (**p** and **q**). The iMAG devices remained fully functional on excretion, confirming their long-term viability in a chronic setting. All the iMAG-decoded distance bars are plotted as mean ± s.d. Also, $n = 3$ for all the distance and error measurements. Furthermore, $n = 4$ for all the signal strength measurements.
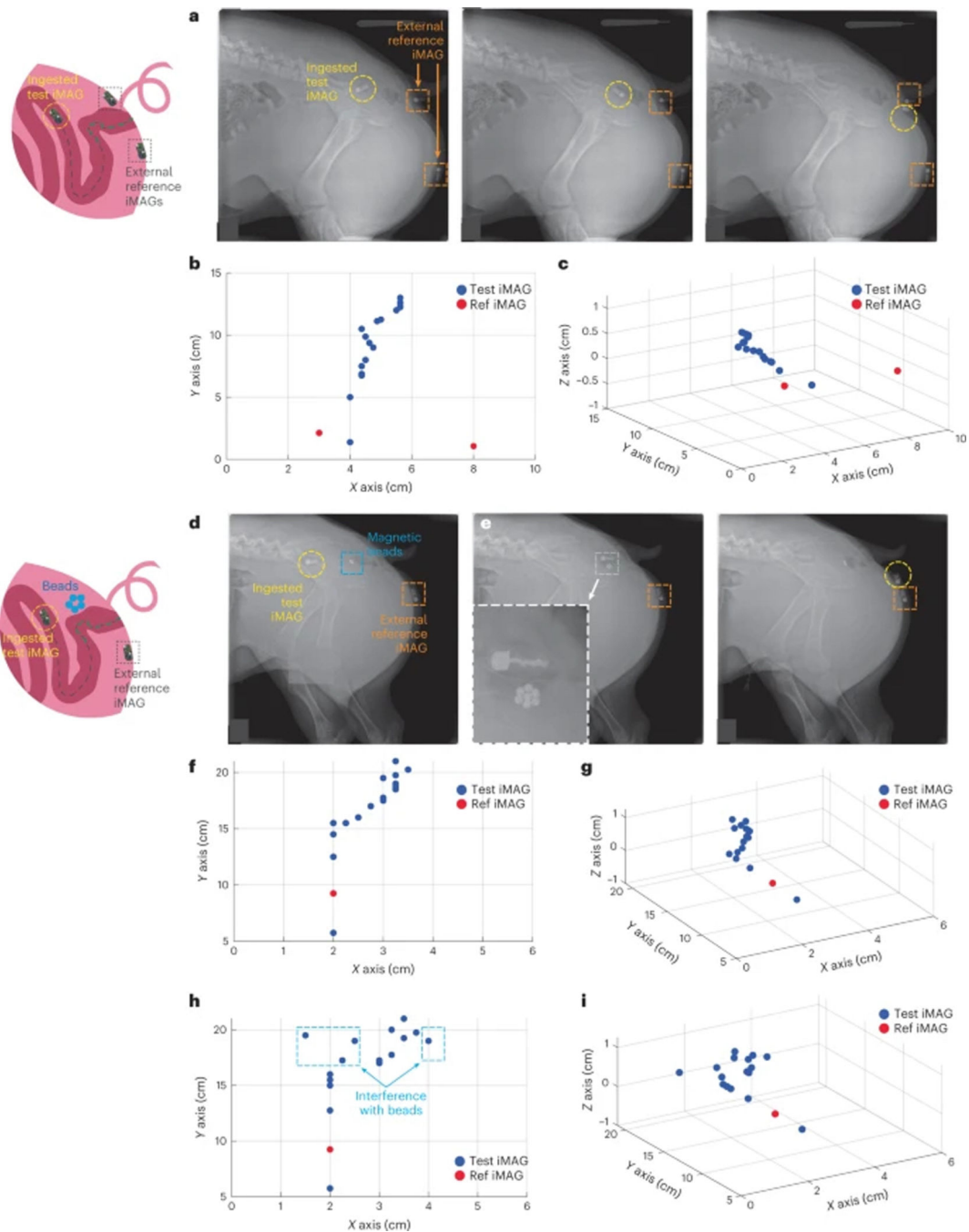
Fig. 5 |. Application of iMAG in FI and magnetic label tracking.
a, The iMAG placed 16 cm proximal to the anal verge of the pig using a catheter and two reference iMAG devices fixed externally on the skin for the evaluation of our FI model. The iMAG was pulled out in increments of 5 mm and a measurement was made at every step to reconstruct the trajectory. **b,c**, Top view (**b**) and side view (**c**) of the reconstructed 3D trajectory, which was successfully mapped to the colonic anatomy. On comparing the decoded distance traversed by the iMAG with the actual distance moved by the catheter, our system serves as an accurate (>97%) indicator of defecation. **d**, Colonic passage study of

the iMAG in the presence of magnetic barium beads to evaluate our system's specificity to magnetic labels. **e**, Placement of barium beads inside a specific location in the colon and their relative position when the iMAG comes close to them during passage. **f,g**, Top view (**f**) and side view (**g**) of the iMAG's trajectory in the absence of barium beads, showing close resemblance to the reconstructed colonic anatomy in b and c for a different pig. **h,i**, Top view (**h**) and side view (**i**) of the trajectory in the presence of barium beads, distinctly showing the errors in the decoded position due to the distortion of magnetic field when the beads are in close proximity (>5 cm in this case) from the iMAG being localized.

Table 1 |

Comparison with existing EM-based tracking methods

System specifications	This work	Ref. [13]	Ref. [16]	Ref. [41]	Ref. [43]	Ref. [55]	Ref. [44]
Localization modality	Magnetic field gradient	MRI inspired	Magnetic tracking	Magnetic tracking	EM-induction-based tracking	MRI gradients	RF-based backscatter
Localization dimension	3D	2D	5D*	3D	6D*	6D*	3D
Mean spatial resolution	1.5 mm **	0.5 mm	2.1 mm	5 mm	<5 mm	2 mm	14 mm
Field of view	$40 \times 40 \times 40$ cm^3 #	1.2 cm ##	$7 \times 7 \times 5$ cm^3	$20 \times 20 \times 20$ cm^3	Hemisphere with 15 cm radius	30 cm from centre	8 cm^3 $
Penetration depth	40 cm #	1.2 cm	5 cm	20 cm	15 cm	Sensor dependent $$	8 cm
Temporal resolution	300 ms	N.R.	5 ms	7.5 ms	33 ms *#	62.5 ms *#	N.R.
Sampling frequency	Once per minute *$	N.R.	200 Hz	133 Hz	30 Hz	16 Hz	N.R.
Sensor size	20 mm length 8 mm diameter	$1.8 \times 1.2 \times 0.3$ mm^3	12.8 mm length 6.4 mm diameter	12 mm length 6 mm diameter	3× (15 mm length, 4 mm diameter)	N.R.	7.5-cm-long antenna
Sensor communication	Wireless	Wireless	N/A	N/A	Wireless	Wired	Wireless
Sensor power	Battery	Wired	N/A	N/A	N/A	Wired	N/A
Multi-sensor localization	Yes	Yes	No	No	Yes	No	Yes
Field generator	Planar electromagnets (B 15 mT)	Strong permanent magnets (0.2–1.0 T)	N/A	N/A	EM coil with modulated current	Volume-enclosing MRI gradient coils (B > 1 T)	External transmitter array (830–870 MHz)
System safety	Yes	No (sub-Tesla-level B)	Yes	Yes	Yes	No (strong B, invasive sensor)	Yes
System evaluation	In vivo (large animal model)	In vivo (small animal model)	Bench study (outside organisms)	In vivo (large animal model)	Bench study (outside organisms)	N.R.	Tissue phantoms and ex vivo

*
Angular orientation is also reported (3D + 2D/3D).

**
Scalable with gradient strength and sensor resolution.

#
Scalable with coil size and current.

##
Reported for a single axis.

$
Only depth FOV is relevant for RF.

$$
Depends on penetration depth of the wired sensor.

*#Converted from the reported sampling frequency.

*$Sufficient for GI tract; can be increased to 3.3 Hz. N.R., not reported. N/A, not applicable.